UNIVERSITY OF FLORIDA

2005-06 FINAL ANNUAL
University Research Program in Robotics REPORT
Submitted: November 30, 2006

Contract No.:	**DE-FG52-2004-NA25588**
Contract Period:	01 September 2005 – 31 August 2006
Project Manager:	Syed Zaidi, NA-115.2, NNSA URPR Program Manager
Principle Investigator:	James S. Tulenko, Nuclear & Radiological Engineering
Co-Principle Investigator	Carl Crane III, Mechanical and Aerospace Engineering

4.0 LEVEL-1 MILESTONE FOR URPR

Develop advanced robotic mobility, mapping, handling, simulation and safety technology to support Stockpile Stewardship.

The University Research Program in Robotics (URPR) Implementation Plan establishes a roadmap for an integrated group of universities to perform fundamental research that addresses broad-based robotics and automation needs of the NNSA Directed Stockpile Work (DSW) and Engineering Campaigns.

4.1 LEVEL-1 MILESTONE FOR UFL

Perform fundamental research in micro-electrical mechanical systems, micro force control and macro force control.

The research performed by the University of Florida (UF) is directed to the development of technologies that can be utilized at a micro-scale in varied environments. Work is focused on micro-scale energy systems, visualization, and mechanical devices. This work will impact the NNSA need related to micro-assembly operations. The URPR activities are executed in a University environment, yet many applications of the resulting technologies may be classified or highly restrictive in nature. The NNSA robotics technologists apply an NNSA needs focus to the URPR research, and actively work to transition relevant research into the deployment projects in which they are involved. This provides a "Research to Development to Application" structure within which innovative research has maximum opportunity for impact without requiring URPR researchers to be involved in specific NNSA projects. URPR researchers need to be aware of the NNSA applications in order to ensure the research being conducted has relevance; the URPR shall rely upon the NNSA sites for direction.

4.2 LEVEL-II: DEVELOPMENT OF NANO-SCALE RADIOISOTOPE BATTERY MODELS AND SUPPORT RADIATION TESTING OF COMPONENTS

4.2.0 Goal/Objective

4.2.1 Objectives

The UF objective, responding to NNSA goals during this twelve month period, is to evaluate conversion technologies for nano-scale radioisotope batteries. Appraisal of radiation capture in extremely small scale devices will utilize fundamental calculations with MCNP5 and EGS Monte Carlo charged-particle transport codes. Calculations will investigate both direct energy conversion pathways and those combined with indirect conversion. The evaluation of luminescent materials for indirect conversion pathways, improving but known to be sensitive to radiation effects, will be coupled with advanced photovoltaic devices featuring improved efficiencies and radiation tolerance. The aim of the UF design team is development of a realistic nano-scale radioisotope battery model that has the potential to provide sufficient power for future MEMS devices.

4.2.1.1 Background

Nanotechnology is an area in which NNSA is making significant investment and represents a radical departure from conventional technologies. The UF research objective originated with the realization that nanotechnology motors need energy and an energy converter employing radioactive disintegration has a very favorable energy density advantage over all other energy sources for creation of nano-scale batteries. Nuclear battery technology saw its beginning around 1913, and has received considerable research attention for applications requiring long-life power sources for space. The scientific principles are well known, but modern nano-scale technology and new wide bandgap semiconductors have created opportunities for new non-thermal devices with interesting material properties not previously available. Novel properties are discovered daily from systems with nano-scale dimensions. Progress in semiconductor fabrication and higher purity / low defect materials continue to produce major advances crucial to MEMS technology. These state-of-the-art accomplishments promise new opportunities to meet the challenging goal of a long-life nano-scale nuclear battery compatible with MEMS motors and power requiring devices. An on-chip MEMS power source may be achievable through this technology.

4.2.1.2 Approach

UF will direct its research experience in radiation effects on electronics and simulation/ calculation capabilities to discover novel approaches leading to the development of a nano-scale radioisotope MEMS battery. The application of radioisotope knowledge in MEMS dimensions requires different approaches and essential modification of former direct-energy conversion radioisotope battery designs. UF research experience in the subtleties of radiation transport and absorption will focus on nanostructures and superlattice solid state devices. This effort seeks refinement of analysis and simulation methods crucial for understanding basic mechanisms in radioisotope nano-battery designs implemented in semiconductor materials. Research at the UF Robotics Lab is focused on the task of understanding through Monte Carlo codes what can and cannot be accomplished in the nanometer realm. Two codes will be compared, the powerful but unwieldy EGSnrc code and the better-known MCNP5 code. Both these codes are routinely used in nuclear engineering and medical physics, but neither code has been extensively used as a tool for

studying nanotechnology systems. UF efforts will be coupled with in-situ irradiation tasks featured in Section 2.2 - Rad-Hard Technologies and Development of MEMS Devices. Key properties and design elements will be tested with available radiation sources to seek proof of concept verifications.

4.2.1.3 Preface

The multi-year goals that rely on the Monte Carlo transport code software tools (MCNP5 & EGFS) for modeling and simulation of charged particle transport in ultra-small scale energy conversion devices are undergoing a degree of proof of concept with selected radiation testing. This scaling down of energy conversion mechanisms, using systems of proven operability in larger existing nuclear batteries, to nano-scale is challenging. UF has focused research activities on investigating different methods to adapt battery conversion mechanisms in greatly reduced dimension space for nanobattery applications. The emphasis of the UF effort is on fundamental research and understanding will lead to development of actual prototypes.

4.2.1.4 Milestones/Deliverables:

2.1.2.1 Run simulations using full emission spectrum radioisotope sources
2.1.2.2 Present research results at ANS 2006 Topical Meeting on Remote Systems
2.1.2.3 Provide annual report of key results

4.2.1.5 Activities and Brief Discussion:

The literature cites radioisotopes such as tritium, nickel-63, promethium-147, and technetium-99 in tests of radioisotopes that produce low energy beta or sometimes alpha particles of varying energies. Health, environmental and limiting harmful Bremsstrahlung radiations are offered as reasons for these choices. These health issues clearly favor Ni-63 for many applications, along with nickel's compatibility with semiconductor fabrication technology. Historically, plutonium-238, curium-242, curium-244, and strontium-90 have been used in radionuclide batteries.

The special limitations faced in micro- and nano-scale systems are absence of shielding for radiation or temperature. This rules out all the mature thermal conversion techniques successfully developed for deep-probe space use. The UF effort, recognizing these limitations, is directed at non-thermal conversion techniques. A review of radioisotope properties for long half-life, alpha or beta emission, and Q-value allows selection of candidate sources for comparison. A table constructed of alpha and beta emitters with long half-lives is shown below (Table – 4.2.1.3.1).

Table 4.2.1.3.1 – Long Half-Life Alpha and Beta Radionuclides

Isotope	Density	Activity	Ci Density	Half-Life	Q-Value	Emission
H-3	0.099	9610	951.4	12.33	180594	β
Ar-42	0.86	258.9	222.7	32.9	599.4	β
Ni-63	8.9	56.7	504.6	100.1	66.945	β
Kr-85	1.74	391.3	681.0	10.756	687.1	β
Sr-90	2.54	138.1	350.8	28.79	546	β
Cs-137	1.87	86.81	162.3	30.07	1175.63	β

Sm-151	7.52	26.31	197.9	90	76.7	β
Pb-210	11.35	76.32	866.2	22.3	63.5	α & β
Ac-227	10.07	72.3	728.1	21.775	44.8	α & β
U-232	18.95	22.35	423.5	68.9	5413.55	α
Pu-238	19.84	17.12	339.7	87.7	5593.2	α
Pu-241	19.84	103.3	2049.5	14.35	20.82	α & β
Cm-244	13.5	80.9	1092.2	18.10	5901.61	α
Cf-250	15.1	109.3	1650.4	13.08	6128.44	α
Cf-252	15.1	536.5	8101.2	2.645	6216.87	α
	g/cm^3	Ci/g	Ci/cm^3	Years	KeV	Particle

Table 4.2.1.3.1 – Long Half-Life Alpha and Beta Radionuclides

A noticeable trade off in half-life versus energy density is revealed. The high alpha energies, normally between 5 and 6.5 MeV, are limited in penetration and have modest half-lives. The doubly charges alpha particle has strong coulombic interaction with the crystalline lattice, follows a mainly straight line penetration path and deposits the majority of its energy near the end of the penetration range. Alpha source designs utilizing semiconductor technology are possible, but damage thresholds, heating effects and radiation tolerance are important issues. The pure beta emitters, in general, have higher penetration ranges. Design challenges center on radiation absorption in the source and the active region of the semiconductor device. The charged beta particle also transfers energy via coulombic interactions with the crystalline lattice. However, the beta interaction is plainly different from alpha particles. Each interaction follows a highly erratic path and can transfer all, some or none of the energy. The greater penetration range allows multiple stacked cell designs not possible with the shallow penetrating alpha particles.

The UF team has conducted a number of candidate simulations and analyses of key source configurations to develop important design specifications. Many published articles only use the average (typically 1/3 the maximum energy for betas) energy for their modeling. Designs in planar semiconductor technology benefit from a complete analysis using the true energy spectrum of the radionuclide source. Essential knowledge for optimization of the source is realized by this full energy spectrum simulation. MCNP5 based analysis in the micro-scale provides the fundamental relationships among: thickness versus source self-absorption, power versus energy density (source size), edge losses versus thickness (source geometry), and heating (temperature and heat transfer characteristics).

UF prototype models continue to be refined by utilizing recent developments that include: improvements in materials and their properties, fabrication technology breakthroughs (3-D geometries), simulated efficiencies (MCNP5 calculations), and information gained through radiation tolerance testing (UF Cobalt-60 Irradiation Facility). Developments in indirect conversion technology, most notably radiation tolerance of fluorescent/phosphorescent polymer materials, appear promising. These changes have the potential to capitalize on the progress in photovoltaic devices featuring higher efficiencies and higher radiation-tolerant wide band-gap materials.

4.2.1.6 Outcomes

Examples of the value of analysis and simulations using MCNP5 and EGS software can be demonstrated by findings for Nickel-63. Nickel-63 radioisotope was studied as a source that is a

pure beta emitter. Monte Carlo charged transport code was used to determine parameters featuring optimization of the source with a simple pn-junction direct energy converter with its junction located 1μm below the planar surface interface with the radionuclide source. The maximum energy converted and highest efficiency was shown to be for a source that is only 0.7μm thick. This calculation used the accurate nickel-63 energy spectrum and not just the average energy. Precise values of self-absorption, determination of the energy spectrum transmitted through the source/device interface, and amount of charge stopping within a diffusion length of the pn-junction space charge region were calculated. An efficiency of 7.4% was determined for this configuration with a silicon device.

Other calculations examined the relationship of the source edge loses versus planar area size. Edge loses for planar geometries smaller that 2 μm on a side where determined a controlling factor for source thicknesses below 1 μm. Additional calculations using these specifications revealed that it was possible to stack three individual conversion devices so that each receives a portion of the fairly penetrating nickel source betas. The doping of the second and third pn-junction devices required appropriate decreases to increase the active collection volume and match current (power) capacities of all three devices connected in series. The built-in voltages will be slightly different, but matching of the series current is mandatory. These results are currently reflected in the ongoing development of a prototype model based on indirect-conversion mechanisms.

The UF design team is pursuing a major improvement using a nano-scale radioisotope battery conversion system, based on indirect-conversion mechanisms, by using stacked conversion cells of heterogeneous materials (shown in Figure 4.2.1.4.1). The UF team has been evaluating solutions to the critical challenge presented by interconnect technology. A potential solution for increasing the power output of miniature planar devices may be achieved through 3-D architectures.

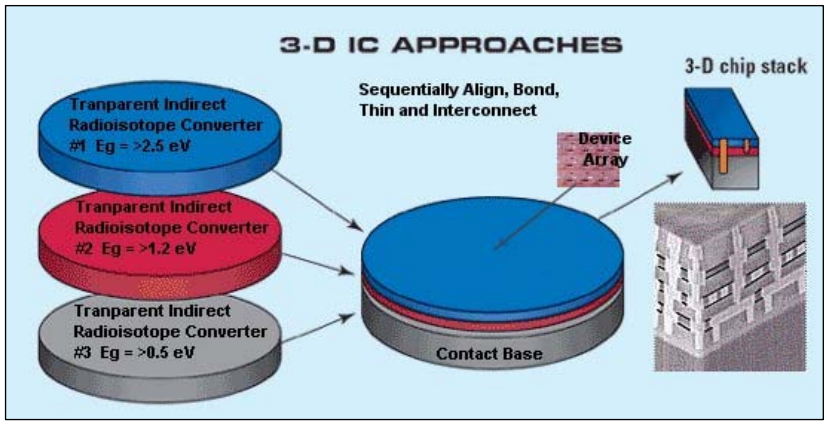

Figure 4.2.1.4.1 – General Concept for Indirect-Conversion 3-D Approaches

Radioisotope emissions penetrate deeper than nano-scale dimensions, and a 3-D stack of conversion devices have the potential to provide additional output power within the limited planar geometry. This in effect increases the total conversion efficiency for a single source, and would be doubled by sandwiching the radioisotope between two 3-D stacked converters. Aligned wafer bonding is a state-of-the-art wafer-to-wafer 3-D interconnect technology that is becoming an established method in MEMS manufacturing. These through-die interconnections reduce critical connection lengths, thereby decreasing losses and other unwanted parasitic effects. This evolving interconnect method holds promise to reduce the complexity of fabrication and is a key design feature needed in the development of UF's nano-scale radioisotope battery model.

UF modeling of this arrangement can be demonstrated with the analysis of two-terminal triple-junction cells with a Ge bottom cell, GaAs middle cell and a GaInP top cell. The direct band gaps (Egs) are: 0.8eV, 1.424eV and 1.85 eV, respectively. However, the conclusions will be equally valid for a GaInP/GaAs two-terminal tandem cell, since the Ge bottom cell does not affect the design of the GaInP or GaAs junctions for any reasonable cell design.

Thickness affects the performance of GaInP/GaAs/Ge triplejunction cells, when connected in series. At one extreme, a very thin GaInP top cell will produce almost no photocurrent, so the entire triple junction cell will be photocurrent-limited by the top cell. At the other extreme, a triple-junction cell with a very thick top cell will generally be photocurrent-limited by the middle (GaAs) cell. However, a triple-junction cell must be current matched for optimal performance, the optimal top cell thickness lies between these two extremes, and will depend on the incident spectrum. This last point is very important, and is the focus of modeling for refining radioisotope conversion prototypes and justification in using the complete emission spectrum for designs.

As an example, we simulate the power produced by a triple-junction cell as a function of top cell thickness under illumination by the AM0 standard spectra at 300 K. The AM0 spectrum is most heavily weighted toward photons with energy greater than the GaInP top cell's band gap. Therefore, the optimal top for AM0 is the thinnest. Because the other spectra contain fractionally less of this short-wavelength light, the top cells must be thicker for optimal performance. UF simulations of the photocurrent produced by each cell (GaInP or GaAs) is calculated independently without being current-limited by the other cell. The MCNP5 calculations provide the energy spectrum of the transported photons at the bottom of each cell, and this is used as the source for the cell underneath.

A simplified version of the stacked 3-D arrangement is seen in Figure 4.2.1.4.2, below. The concept is based on a radioisotope source located only on the top. It features the use of a moderator which can be used to either cool the source (reduce the incident kinetic energy) from its high specific activity, or even designed to provide a material with a high absorption of the source with emission of secondary alpha particles, for example. The technology for transparent conducting layers makes possible the stacked interconnection of three independent conversion cells. The last layer might also contain a bottom using a common phosphor with excellent luminescent properties. This would compensate for the phosphors generally limited radiation tolerance and increase the efficiency by acting on any remaining energy making it through the complete stack.

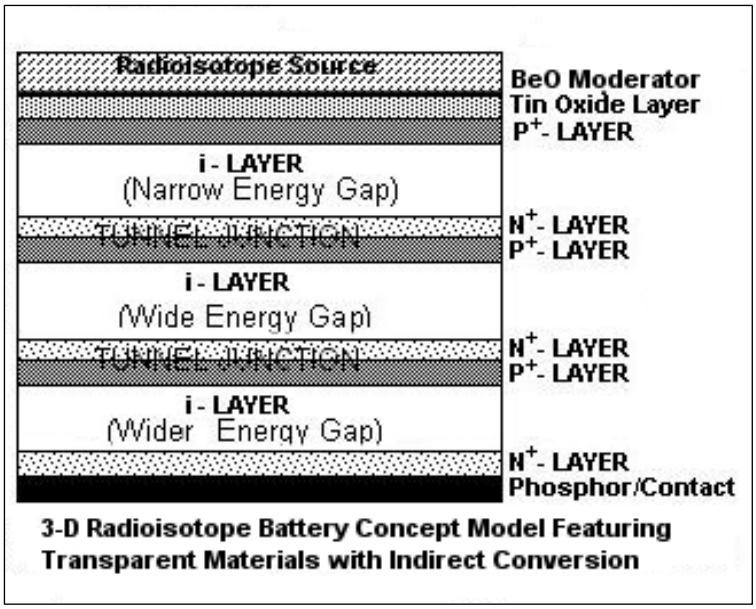

Figure 4.2.1.4.2 – Simplified 3-D Model for Simulation

The UF team is preparing to evaluate a further refinement of this 3-D concept during the next phases of our planned research. We have obtained a radioluminescent Cu^{1+} doped quartz glass from Alan Huston of the Naval Research Labs (NRL). The properties of the glass make it a good candidate to use as a down converter of higher energy photons. The Cu^{1+} ion is excited into the Cu^{2+} state by the incident radiation, and when it returns to its original Cu^{1+} state it emits a green spectrum of photons shown in Figure 4.2.1.4.3.

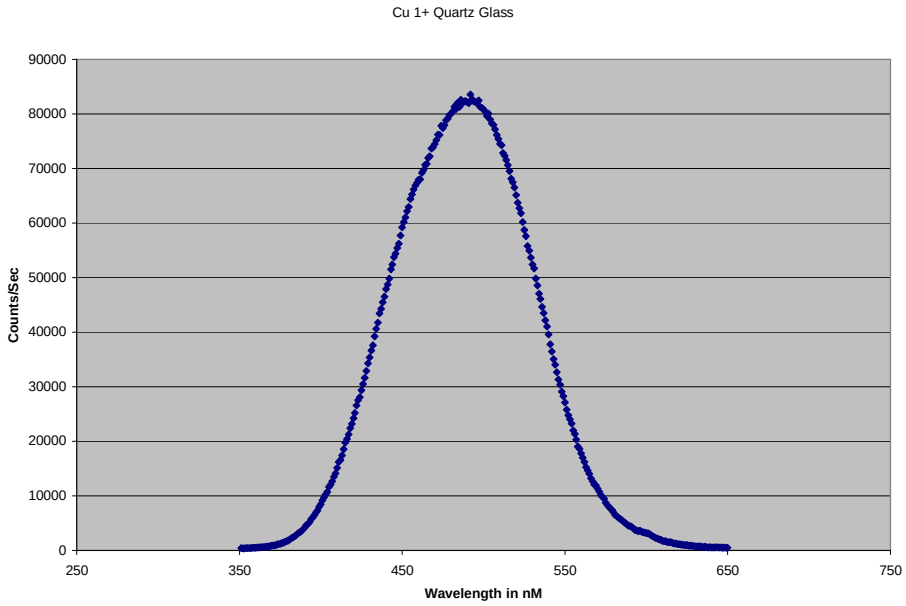

Figure 4.2.1.4.3 – Spectral Emission from Cu^{1+} Doped Quartz Glass

This quartz glass may be used as the substrate for fabricating each individual photovoltaic device. If the radionuclide source is also incorporated into this process, the stacked 3-D

arrangement of cells would benefit from conversion from at least two cells (also the one below in the 3-D stack) of the emitted spectrum. This scheme holds promise because the photovoltaic cells would not be so limited by conversion of only the emitted radioisotope energy within the very thin junction region. Power capacity is then mainly determined by series addition of voltage potential which is easier to fabricate and provides better size reduction. The quartz glass is currently produced in as small as 10μm thicknesses, and is created by standard semiconductor processing technology.

This arrangement is schedule for testing in the UF Cobalt Irradiation Facility. Two different photovoltaic devices will be evaluated using the Cu^{1+} doped quartz glass for down-conversion of the higher kinetic energy photons. These are a $CuInGaSe_2$ (shown in Figure 4.2.1.4.4) and the GaAs PIN (pictured in Figure 4.2.1.4.5) photovoltaic cells with the Cu^{1+} doped quartz glass.

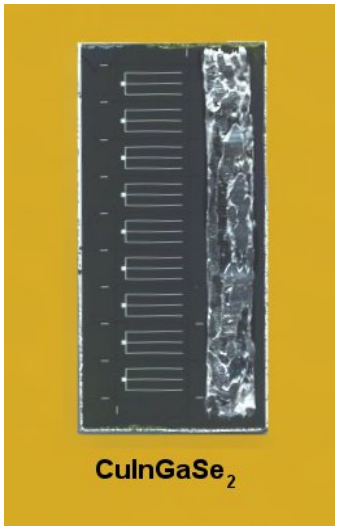

Figure 4.2.1.4.4 Copper Indium Gallium Selenide Photovoltaic Cells

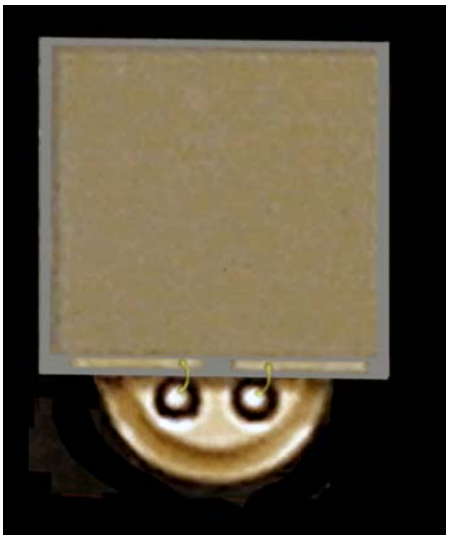

Figure 4.2.1.4.5 Photograph of GaAs PIN Photovoltaic Diode

The CIGS photovoltaic cells were tested for conversion efficiency using an AM 1.5 solar simulator. This uses an ELH (tungsten-halogen bulb) lamp with an integral dichroic rear reflector is utilized as the solar simulator in the experimental setup. Brand name is ELH Lamp (120V, 300W) made by GE. A solar standard is used to calibrate the setup to AM 1.5G with this lamp. The results are shown in Table 4.2.1.4.1, and a representative I-V graph is shown in Figure 4.2.1.4.6.

	CIGS #30			CIGS#22		
Cell Number	4	5	6	4	5	6
Voc, V	0.481663	0.509569	0.495452	0.497835	0.492169	0.496721
Jsc, mA	29.73781	20.69444	19.75695	30.47265	30.80717	29.84617
F.F., %	58.15647	49.94229	41.59096	57.56076	57.35679	56.55816
Eff , %	8.3301	5.0556	4.0712	8.7322	8.696671	8.3849
Vmax, V	0.340679	0.363182	0.332278	0.356402	0.350549	0.351752
Jmax/cm2	22.972	13.213	12.422	24.345	24.614	23.712
Pmax, VmA/cm2	7.825	4.799	4.127	8.677	8.629	8.314

Table 4.2.1.7 – CIGS Photovoltaic AM1.5 Results

The best cell (Figure 4.2.1.4.6) performance produced: a cell voltage of 0.5V, a fill-factor of 58%, an efficiency of 8.7% and a power density of 8.6 nW/cm2.

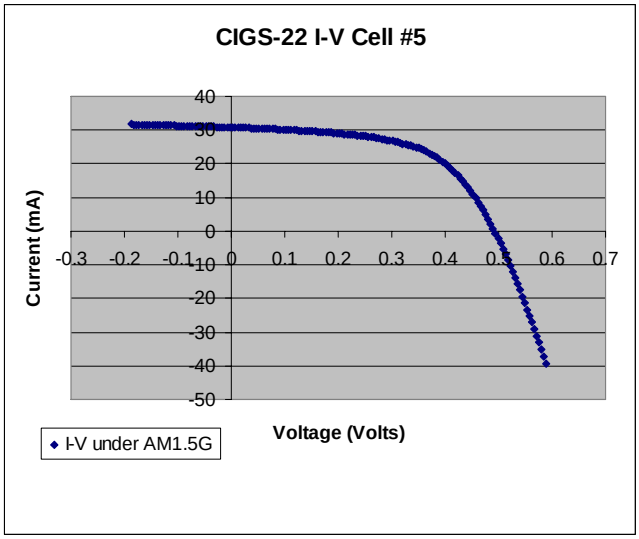

Figure 4.2.1.4.6 – Best CIGS Photovoltaic AM1.5 Performance

4.2.2 Goal/Objective

4.2.2.1 Rad-Hard Technologies and Development of MEMS Devices

This work is in support of the 4.2.1 Nano-Scale Radioisotope Batteries objective by appraising the radiation sensitivity of candidate materials. Radiation sensitivity tests will be planned and

conducted on materials identified for use in the UF prototype radionuclide battery design. Scaling down such energy conversion mechanisms, that may have proven operability in larger existing nuclear batteries to the nano-scale, will be a challenge. The emphasis of the UF effort is on fundamental research and understanding, and using identified key criteria to eliminate inappropriate designs or materials.

4.2.2.2 Preface

The multi-year goals benefit from the outcome of material and basic concept tests to direct the modeling and simulation of prototype ultra-small scale energy conversion devices. UF has focused research activities on investigating different methods to adapt battery conversion mechanisms in greatly reduced dimension space for nanobattery applications. The emphasis of the UF effort is on fundamental research and understanding necessary to develop design specifications for ultra-small power sources needed for MEMS devices.

4.2.2.3 Perform in-situ cobalt irradiation evaluations

4.2.2.4 Activities and Brief Discussion

The UF indirect conversion nano-scale model is supported by some of the most recent irradiation work. A strong candidate material for the photovoltaic conversion for the luminescent conversion of the Cu1+ doped quartz down-converter is GaAs. The irradiation involves characterization and optimization of special unintentionally doped GaAs PIN photovoltaic diodes [Fig. 2.1.4.5] fabricated for the spectral output shown in Fig. 2.1.4.3. This work is leading to verification of the basic principles central to the function of UF's latest indirect conversion nano-scale radioisotope battery prototype. In this work, GaAs-based PIN detectors with mesa sizes 1, 2.5, 5, 7.5 and 10 mm were fabricated and characterized for alpha particle response. A planar Po-210 alpha source (1 cm x 10.4 cm) with a decay rate of 353.72 MBq and alpha energy of 5.4 MeV was used for alpha response measurements of the PIN detectors. Additionally, the alpha response characteristics of the PIN detectors as a function of device area were determined. Dark current levels in the PIN detectors ranged from 6.1 to 9.5 pA at zero bias. Strong alpha response of up to 5 nA/mm^2 with a linear relation between the response current and mesa area was measured.

The basic efficiency and I-V characteristics were measured using a ELH (tungsten-halogen bulb) lamp with an integral dichroic rear reflector is utilized as the solar simulator in the experimental setup. Brand name is ELH Lamp (120V, 300W) made by GE. A solar standard is used to calibrate the setup to AM 1.5G with this lamp. The I-V curves are shown in Figures 4.2.2.3.1 & 4.2.2.3.2, and the characteristics are summarized in Table 4.2.2.3.1. The efficiency of the smaller device is 7.1% with a fill factor of 71%, and is for the complete solar spectrum. This compares very favorable with published data for Ni-63 source tests on materials like Si, GaAs, SiC and GaN. This information will be helpful in establishing the overall efficiency of the UF indirect-conversion radionuclide power prototype when tested with the Cu1+ doped quartz glass energy down-converter from NRL.

The general effects of most alpha or beta radionuclides was modeled by the Po-210 alpha particles which create a large number of electron-hole (e-h) pairs. The e-h pairs are swept away by the built-in potential of the device, generating a response current. One of the large benefits of GaAs PIN devices is the ability to operate them under zero bias – their silicon based Schottky diode counterparts typically require operational voltages of > 100 V [1]. The built-in potential (V_{bi}) of a PIN detector operating in reverse-bias photoconductive mode is given in Equation (0.1).

$$V_{bi} \approx \frac{kT}{q_{e^-}} \ln\left(\frac{N_A N_D}{n_i^2}\right) \tag{0.1}$$

where k is Boltzmann's constant, T is the temperature, q_{e-} is the charge of an electron, and N_A, N_D, and n_i are the densities of the dopants in the p-layer, the n-layer, and the intrinsic layer, respectively. Given that $N_A=2\cdot10^{19}/cm^3$, $N_D=4.4\cdot10^{18}/cm^3$, and $n_i\sim10^{15}/cm^3$, the built-in potential of our GaAs detectors is calculated to be about 1.1 V from Equation (0.1), resulting in a field across the intrinsic region of roughly 2.2 kV/cm at zero bias.

The responsivity of the devices [Amps per particles per second] is given in Equation (0.2).

$$\Re = \frac{J}{\Phi_\alpha} \tag{0.2}$$

where J is the response current per mesa area [Amps·mm^{-2}] and Φ_α is the alpha particle flux on the device surface [particles·mm^{-2}·s^{-1}]. The minimum device area required for a desired response current, $I_{response}$, is

$$A = \frac{I_{response}}{\Re\Phi_\alpha} \tag{0.3}$$

Our GaAs PIN structures were grown by metal-organic chemical vapor deposition (MOCVD) on 2" GaAs:Si substrates. The PIN structure consisted of a 5 μm GaAs:uid intrinsic layer within the p and n-type GaAs top and bottom epilayer regions, respectively. Square GaAs PIN diodes of increasing area were fabricated with mesa side lengths 1, 2.5, 5, 7.5 and 10 mm. Standard Ti/Pt/Au and Ni/Ge/Au metallizations were defined using lithography for the p and n-type ohmic contacts, respectively. A meshed geometry was used for the p-contact in order to increase the bare surface area of the PIN detectors.

Current-voltage measurements were taken in darkness using a four-point probe technique and a Keithley 2400 source meter for low noise. All measurements for alpha response were conducted using PIN devices that were mounted on TO-46 headers using silver epoxy and standard gold wire bonding.

Figure 4.2.2.3.1 shows the dark current and alpha response current measurements for a typical 5 mm device. The device has low dark current (10.6 pA at zero bias), and a strong alpha response (99.4 nA at zero bias). The current levels do not change appreciably with bias voltage; therefore there are no apparent benefits to running the detector at a reverse bias instead of zero bias.

The measured dark current as a function of mesa size is given in Figure 4.2.2.3.2. The dark current increases an average of 39.6 pA/mm as mesa size is increased, as shown by the slope of the linear fit in Figure 4.2.2.3.2. The linear relation between mesa size and dark current indicates that the dominant parameter is the side wall length rather than the area. This is due to surface states on the mesa sidewall that provide current leakage routes [2,3]. There was no passivation of the sidewalls during fabrication, but future work to decrease the dark current levels will include using a sulfur treatment [4] to passivate these surface states.

The alpha response current as a function of device area is shown in Figure 4.2.2.3.3 from the planar Po-210 alpha source (1 cm x 10.4 cm) with a decay rate of 353.72 MBq and alpha energy of 5.4 MeV. A strong alpha response was observed for all device sizes. A linear relation between alpha response and detector area was observed, as expected, since the flux of alpha particles on the detector surface increases linearly with area. The average alpha response current per area is 4 nA/mm^2, as shown by the slope of the linear fit in Figure 4.2.2.3.3. The alpha flux on the detector is estimated to be 3.4 x 10^7 particles·cm^{-2}·s^{-1} from Equation (0.4).

$$\Phi_\alpha = \Gamma \frac{A_{\det ector}}{A_{source}} \qquad (0.4)$$

where Γ is the total decay rate of the source, $A_{detector}$ is the detector area, and A_{source} is the source area. From Equation (0.2), the responsivity of the devices is found to be 0.005 pA·s per alpha particle.

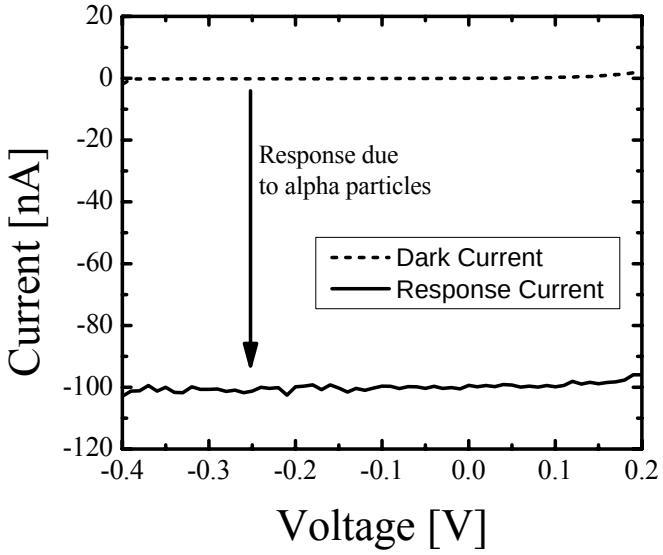

Figure 4.2.2.3.1: Alpha response current vs. bias voltage for a single 5 mm device. The dark current vs. bias voltage is included for comparison.

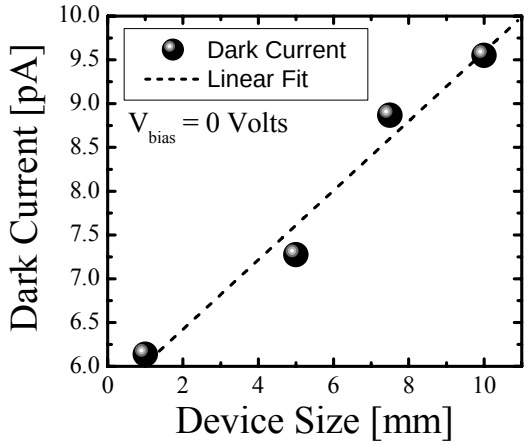

Figure 4.2.2.3.2: Dark current as a function of mesa size at zero bias. The linear relation indicates that the dominant source for leakage current is mesa sidewall states rather than bulk crystal defects.

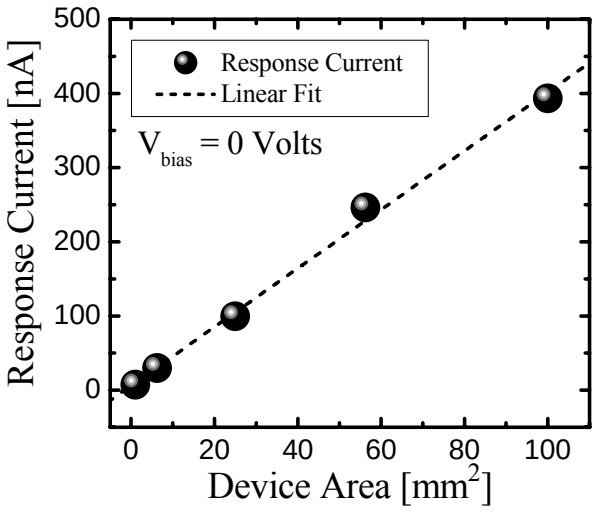

Figure 4.2.2.3.3: Alpha response current as a function of device area at zero bias. Response current is found to be linearly dependent on device area.

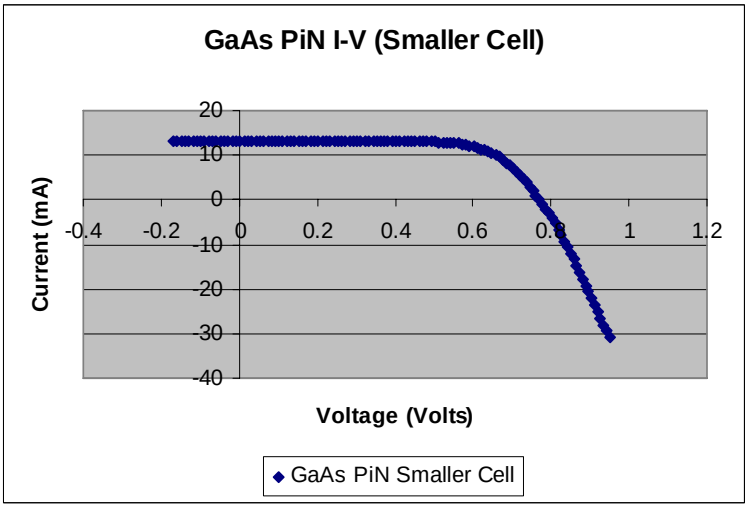

Figure 4.2.2.3.4 – AM1.5 Characterization of 250µm GaAs PIN

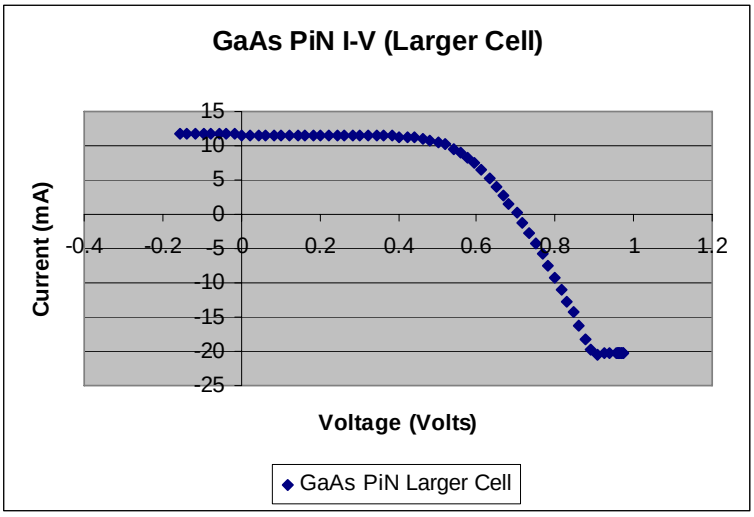

Figure 4.2.2.3.5 – AM1.5 Characterization of 500µm GaAs PIN

GaAs PIN	250µm GaAs	500µm GaAs
Voc, V	0.770578	0.704585
Jsc, mA	13.23531	11.61414
F.F., %	70.74885	63.08086
Eff , %	7.2156	5.162
Vmax, V	0.581473	0.520946
Jmax/cm2	12.274	10.131
Pmax, VmA/cm2	7.137	5.278

Table 4.2.2.3.1 – GaAs PIN Properties from AM1.5 Characterization 4.2.2.4 Outcomes

The preliminary fabrication, characterization and verification of operational conditions were completed. The important properties of the photovoltaic devices are as follows: dark current levels in the GaAs PIN photovoltaic detectors ranged from 6.1 to 9.5 pA at zero bias, a strong alpha response of up to 5 nA/mm^2 with a linear relation between the response current and mesa area was measured, and the responsivity of the devices is found to be 0.005 pA·s per alpha particle. These devices are next scheduled to be evaluated with the Cu^{1+} doped quartz glass obtained from NRL in the UF Cobalt Irradiation Facility.

4.2.3 References

[1] G. Bruckner, A. Czermak, H. Rauch, P. Weilhammer, *Nucl. Instrum. Methods* A 424, 183–189 (1999).
[2] Y. Y. H. Qian, S. An, I. Betty, R. Rousina-Webb, E. Griswold, R. Foster, and R. Driad, J. Vac. Sci. Tech. A 22, 1062 (2004).
[3] S. A. Tabatabaei, G. A. Porkolab, S. Agarwala, F. G. Johnson, S. A. Merritt, O. King, M. Dagenais, Y. J. Chen, and D. R. Stone, Mater. Res. Soc. Symp. Proc. 477, 317 (1997).
[4] X.Y. Hou, W. Z. Cai, Z.Q. He, P.H. Hao, Z.S. Li, X.M. Ding, and X. Wang, Appl. Phys. Lett. 60 (18), 2252 (1992).

4.3 UF-2: VISUALIZATION FOR QUALITY ASSURANCE OF MEMS MICRO-ASSEMBLIES

4.3.1 Area 1: Visualization Simulation

The National Nuclear Security Administration (NNSA) relies on employing high technology devices and components to execute its mission and ensure national security. There is a clear emphasis toward the miniaturization of many of these devices, with an emphasis on the development on Micro-Electro-Mechanical Systems (MEMS). As the scale of fabrication of MEMS devices decreases, the level of sophistication of device architecture and operations continues to increase. As MEMS device architecture expands to complex three-dimensional structures, tools to monitor the assembly process, device functionality, tolerances and wear become increasingly important. Traditional optical and scanning electron micrographs (SEM) provide only planar information and the electron beams used in SEM can damage delicate structures. The extremely small physical size of MEMS presents multiple challenges for visualizing these devices without damaging sensitive surfaces and structures. We explore the development of visualization tools based on Micro-Computed Tomography (micro-CT) techniques that permit the three-dimensional visualization and quantitative assessment of these microscopic devices.

Tasks related to the advanced visualization techniques for micro electro-mechanical systems (MEMS) have proceeded throughout the year. The tasks are proceeding along two complimentary approaches that are aimed at ultimately providing optimized micro-CT techniques for the 3-D visualization of advanced MEMS structures. Area 1 focuses on the development of simulation tools that can be used to optimize the parameters for micro-CT visualization of MEMS devices. Area 2 focuses on the empirical development and demonstration of radiographic and micro-CT techniques for the visualization of MEMS devices. The current year's emphasis focused primarily on Area 2, Empirical Visualization of MEMS.

4.3.2 Accomplishments

Simulations were previously run in the IDL computing language in order to determine the optimal materials, beam energies, reconstruction filter, and interpolation method the simulations were run using a sample MEMS device, and results indicated that metallic compounds such as nickel and silver yielded the best contrast, while materials such as Teflon and PMMA (acrylic) are only visible at energies below 30 keV. As part of this periods work, the simulation software was transferred to the Matlab computing platform in order to provide improved flexibility for the further advancement of the simulations and comparison with the empirical data. Simulations were subsequently run on reconstruction methods to optimize contrast in MEMS devices. It was found that LP Cosine and Hamming filters, coupled with a linear interpolation method produced the highest signal to noise ratio. These results are then compared to reconstructions of actual MEMS devices imaged with a micro-CT scanner.

The raw and reconstructed data from empirical micro-CT scans (described in detail in Area 2: Empirical Visualization of MEMS) was imported into Matlab in order to verify the previous simulations regarding optimal reconstruction methods. In order to perform these tests, the raw sinogram data was reconstructed with several available filters and interpolation methods. A contrast to noise ratio was calculated for each filter and interpolation method in the same manner as was done for the initial simulations. The values of the contrast to noise ratios were then compared to determine the optimal settings for image reconstruction. The results of these tests are shown in Figures 4.3.1-1 and -2.

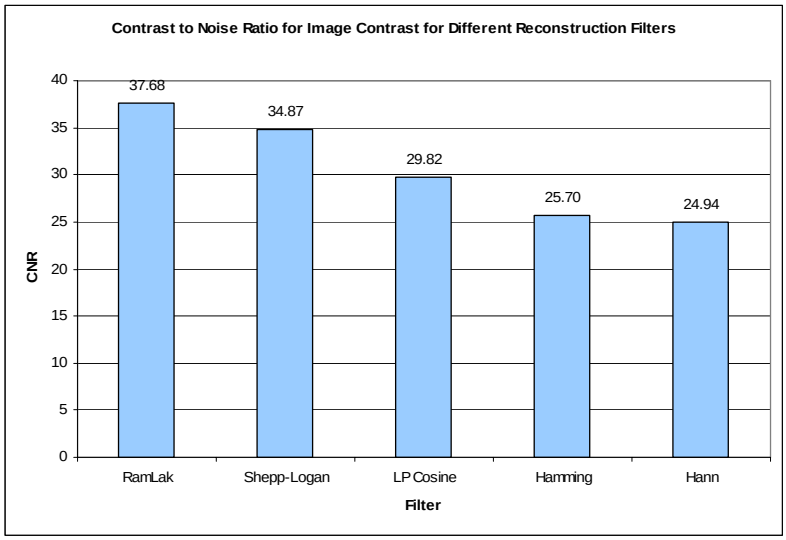

Figure 4.3.1-1. Effect of reconstruction filter on image contrast

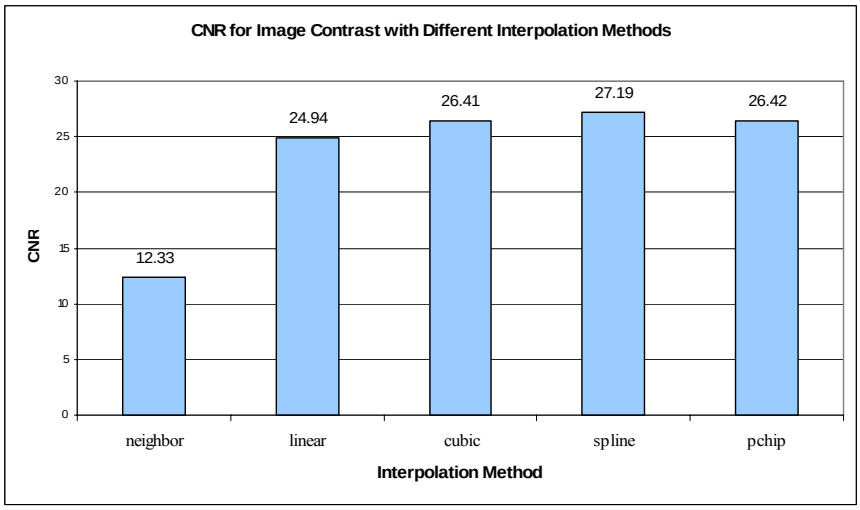

Figure 4.3.1-2. Effect of interpolation method on image contrast

As shown in Figure 4.3.1-1, the Ram-Lak and Shepp-Logan reconstruction filters provided the best image contrast, with all filters having exceptional contrast to noise ratios. All filters used in the tests on the micro-CT scanned images showed improved contrast over what was expected from the previous simulations. These results show promise for micro-CT as a method of imaging MEMS devices. The high levels of contrast to noise ratio indicate a sharp boundary along the edges of the MEMS components in the reconstructed images. Such boundaries allow for better viewing of the overall structure of the components with no loss of clarity due to blurring from reconstruction.

The results of the interpolation method study show that almost all methods provide a similar level of image contrast with only the nearest-neighbor method showing significantly lower contrast. Previous simulations showed that a linear interpolation method provided the highest levels of contrast, but similarly showed no large deviation between methods, indicating that the choice of interpolation method does not have a significant effect on image contrast in reconstructed micro-CT images.

4.3.3 Area 2: Empirical Visualization

Several MEMS components fabricated using LIGA techniques were obtained from Sandia National Labs (SNL) in order to validate the Matlab simulations. LIGA (an acronym from the German words for lithography, electroplating, and molding) techniques involve creating masks using high-Z materials, which are then used along with highly parallel x-ray beams to make molds in PMMA (acrylic). Metals are then electroplated in the molds to create micron-scale components. The SNL samples are made of Ni-alloy, and incorporate features spanning a wide range of spatial dimensions from approximately 1 to100μm. Microscope images of the samples are shown below in Figures 4.3.1-3 and -4.

Figure 4.3.1-3: Optical images of Several MEMS samples from SNL, shown with a micron scale on the left.

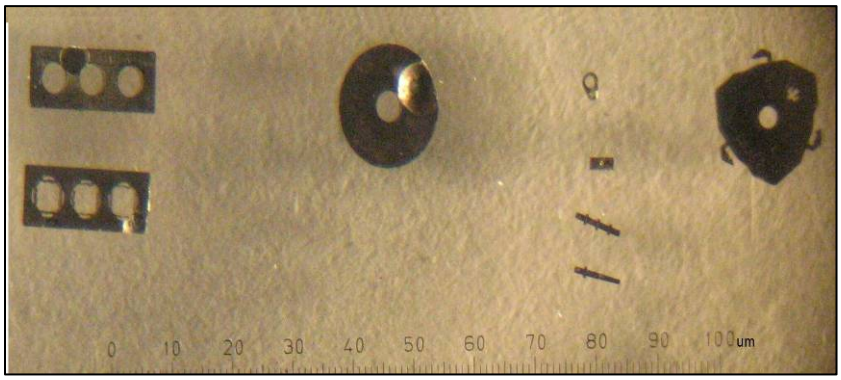

Figure 4.3.1-4: Optical images of additional MEMS components from SNL

The SNL MEMS components underwent micro-CT scanning at Scanco Medical® (Southeastern, PA) with a micro-CT system. All samples were scanned at both 45 and 70 kVp. The micro-CT system used can be operated with a resolution of 6 or 12 microns. Data from these scans was provided in the form of both raw, sinogram data from the scans as well as the reconstructed slices from each component. These data sets were used to create 3D renderings of the components. Samples of the raw data, reconstructions, and 3D renderings are provided below.

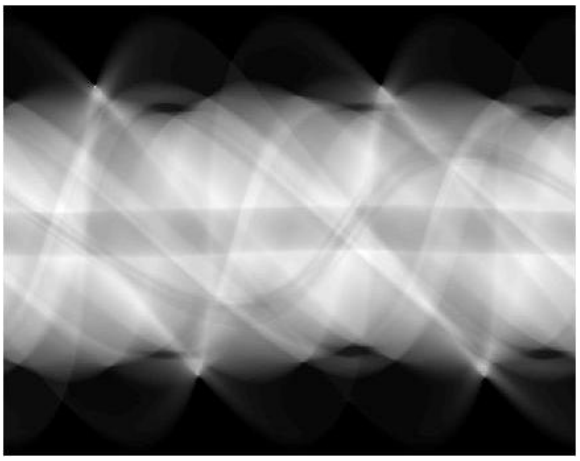

Figure 4.3.1-5: Raw sinogram data from micro-CT scan of MEMS component

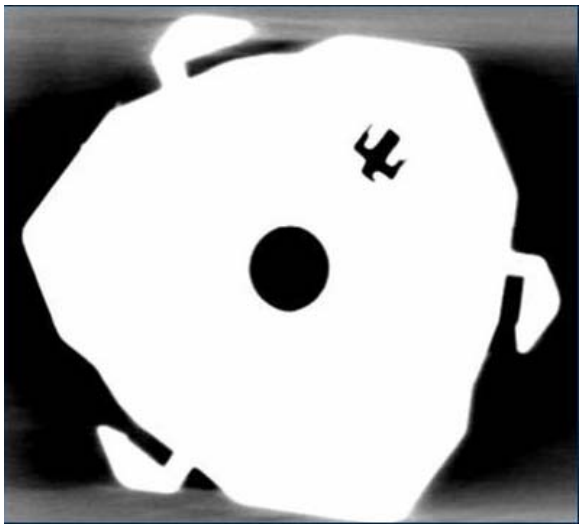

Figure 4.3.1-6: Slice of MEMS component reconstructed from the sinogram illustrated in Figure 4.3.1-5.

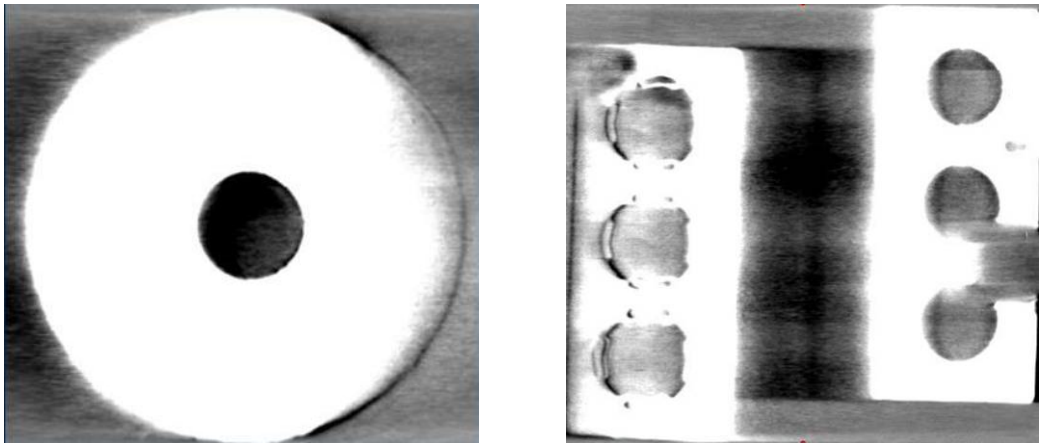

Figure 4.3.1-7: Reconstructed slice of MEMS components

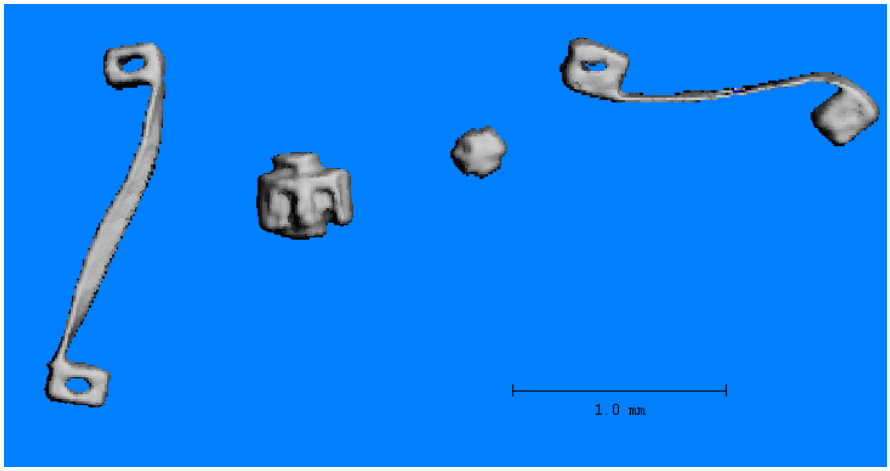

Figure 4.3.1-8: 3-D rendering of several small MEMS components

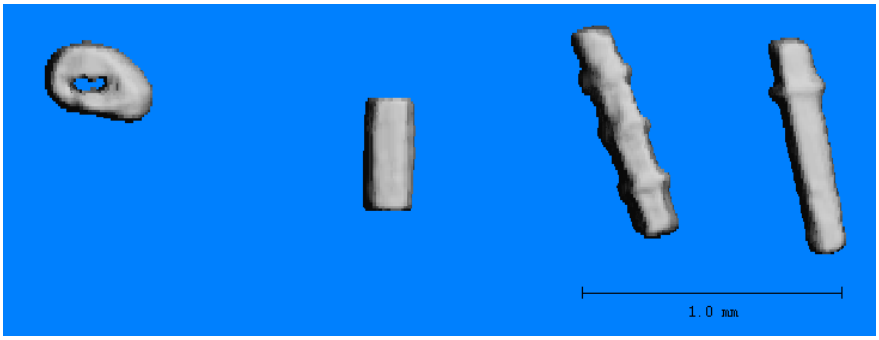

Figure 4.3.1-9: 3-D rendering of smaller MEMS components

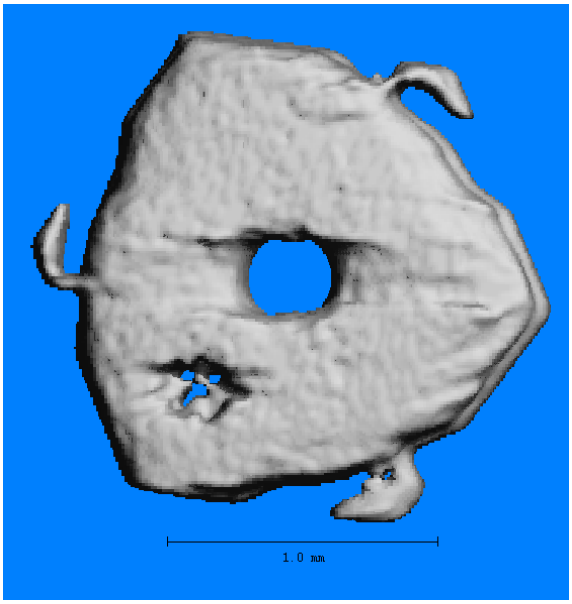

4.3.1 Figure 4.3.1-10: 3-D rendering of MEMS component

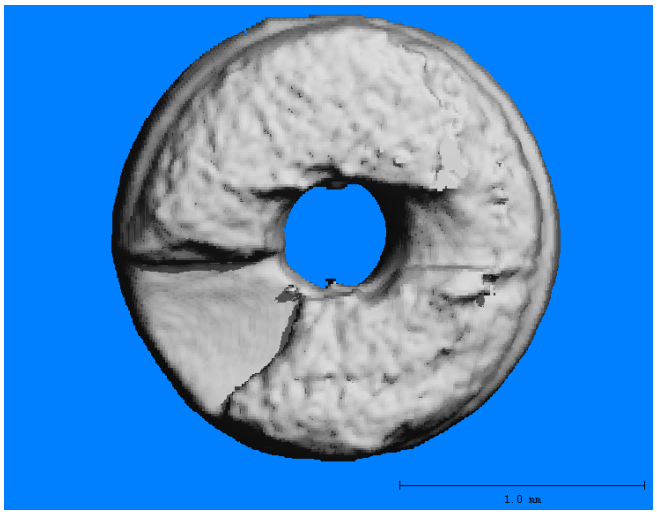

Figure 4.3.1-11: 3-D rendering of MEMS component

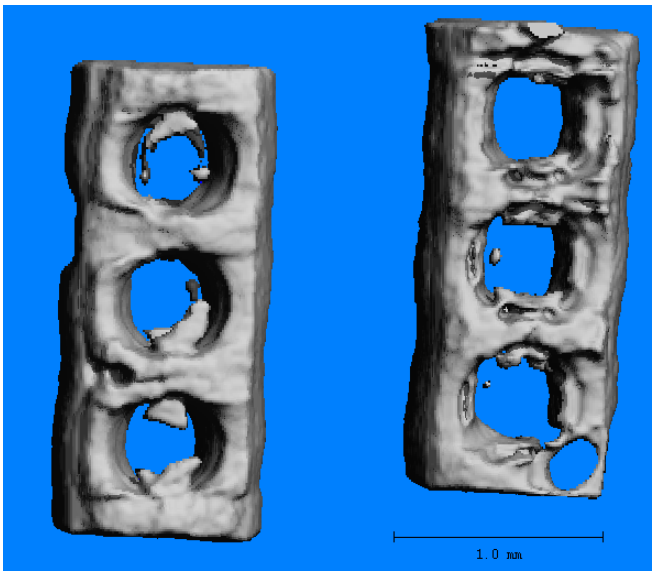

4.3.1 Figure 4.3.1-12: 3-D rendering of MEMS component

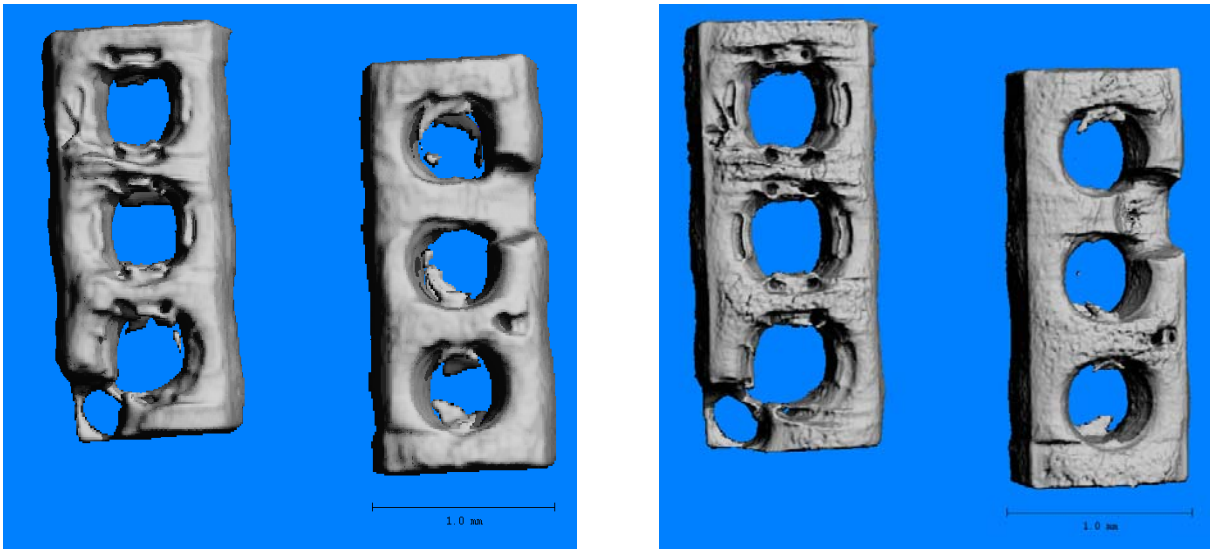

Figure 4.3.1-13: Comparison of normal (left) and high (right) resolution reconstructions on the same MEMS components

As can be seen in the reconstructed images, micro-CT imaging at the lower resolution setting provides a spatial resolution of approximately 10 microns in planar reconstructions. The true value of micro-CT as an evaluative method for MEMS quality assurance is seen in the 3D rendered images. These renderings provide exceptional clarity of each component's overall structure and features, such as the helical twists in Figure 8, and the notch in the circular disc in Figure 10. Such features are difficult, if not impossible to visualize, while looking at projection or slice images of the components such as seen in Figures 4.3.1-7 and -8.

Differences in resolution settings of the micro-CT scanner are shown in Figure 4.3.1-13, with the lower resolution (12 micron) reconstructed image shown on the left, and the higher resolution (6 micron) setting shown on the right. As would be expected, finer details, such as the machining around the holes of the left brick, are more clearly visible at the higher resolution setting. It should be noted that the overall structure of the component is readily visible at each resolution setting, and the choice of resolution depends entirely on the required level of detail in the reconstruction. If the purpose of the micro-CT imaging is only for larger scale checks on proper MEMS construction then a higher resolution system would not be required as all needed information is provided at a lower resolution scan. It follows that if finer details of component construction are required a higher resolution scanner would be required.

The limits of resolution in micro-CT imaging of MEMS components is seen in Figure 4.3.1-9. These components represent the smallest of those provided by SNL, which can be seen grouped together in Figure 4.3.1-2 between the two disc shaped components. As seen in Figure 4.3.1-9, while overall structures are visible, the finer details of the pieces are not readily discernible, such as the holes in the center of the two leftmost pieces in the reconstructed images. It should be noted that these reconstructions were made at the 12 micron resolution, as data for these pieces at the 6 micron resolution was not available. These reconstructions again illustrate the need to know the level of detail required in reconstructions so that appropriate resolution settings can be chosen for a scan.

There does not appear to be a noticeable difference in image quality when comparing reconstructions from the 70keV compared to the 45 keV scans, although only data from the triangular disc component shown in Figures 4.3.1-6 and -9 was available at both energies. Further

testing of multiple components at various energies would be necessary in order to determine the effects of beam energy on image resolution and contrast. It should also be noted that most commercially available micro-CT scanners, such as those utilized by Scanco, can only operate at preset, discrete beam energy settings, and, depending on the specific model, sometimes only a single setting is available. Such features would need to be taken into consideration before purchasing a micro-CT scanner as beam energy may need to be varied for visualization of components made of different materials. As was reported in the last annual report, simulations show that MEMS components constructed of low-Z materials such as PMMA would be better visualized at energies below 30 keV, while the results of these studies show that metallic components can be visualized at 70 keV.

A micrometer-scale image quality phantom has been designed as a known, standardized, test object to demonstrate the functionality and limits of Micro-Computed Tomography (micro-CT) for the visualization of similar Micro-Electro-Mechanical Systems (MEMS) and to provide optimized micro-CT techniques for the 3-D visualization of advanced MEMS structures. The development of an image quality phantom dedicated to micro-CT will aid in the assessment of an imaging system's capabilities and tolerances.

The micro-CT image quality test object was designed as a comprehensive evaluation of a micro-CT system's performance, much in the same way that current clinical quality assurance (QA) programs test the functionality and limitations of clinical computer tomography[1,2]. The test modules of the micro-CT image quality phantom aim at quantifying a system's sensitivity in regards to low contrast detection as well as consistency in both spatial uniformity and resolution.

The phantom itself consists of four separate test modules, each 50μm thick and 200μm in diameter, for a total phantom height of 200μm (Figure 4.3.1-2). Each micron-scale phantom segment is etched to its design specifications from a 200μm thick silicon (ρ= 2.32 g/cm^3) wafer. Aside from the spatial uniformity module, the remaining test modules contain test objects (or voids) that are further etched in the pattern of the above described photomask. The remaining three tests include two separate assessments of low contrast sensitivity, and an evaluation of a system's spatial resolution.

The fundamental measurement of CT-scanners is narrow beam transmission resulting in a cross sectional reconstruction of numbers presumably related to the x-ray linear attenuation coefficient, μ. The linear attenuation coefficients depend upon physical density (grams/cm^3), atomic composition, and photon energy[1].

The uniformity test is a simple and direct approach to determining the accuracy of a system's reconstruction process. To evaluate scan plane uniformity, a test object with appropriate dimensions and uniform attenuation is scanned under simulated conditions[2]. The image quality phantom's uniform silicon test module has a diameter of 50μm and a thickness of 50μm.

The field uniformity test is performed by determining the average CT number in specifically selected regions of interest (ROI) in the image plane. First, an average CT number from an ROI of ~10μm^2 in the center of the phantom is ascertained, followed by measurements at four locations of the phantom's periphery (top, bottom, right, and left). The non-uniformity of the periphery is then presented as the percent difference of the value measured in the center. Non-uniformity which worsens with slice width suggests a scatter effect[4], while non-uniformity with change of phantom size or shape suggests inadequacy of the software uniformity correction[2].

The visibility of low contrast objects is constrained mainly by the amplitude and frequency characteristics of the image noise. The ability to visualize low-contrast objects is the essence of contrast resolution. Better contrast resolution implies that more subtle objects can be routinely seen on an image. The difference of the attenuation coefficients between the object and its surrounding region must be established. This subject contrast is simply the difference in average CT numbers

between two adjacent regions of the image[3]. The sensitivity of a CT scanner can thus be defined in two ways: (1) the minimum detectable difference of attenuation coefficients for a given object size and (2) the smallest size circular object detectable[1].

The second image quality test module evaluates the first definition of low contrast sensitivity. The minimal detectable difference in object attenuation is tested by comparing regions of interest of small test objects to an ROI of the silicon phantom material of equal area. Initially an ROI from the center of the phantom is ascertained. Next ROIs are recorded for the five test objects (cylindrical voids) in the phantom module. The test objects are etched from the original phantom depth and include cylinders of five equally decreasing increments, 10µm to 50µm (the depth of the module itself), each 20µm in diameter.

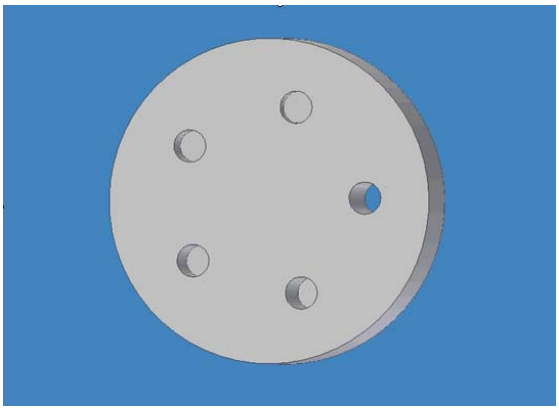

Figure 4.3.1-14: Visualization of the low-contrast sensitivity module.

The next module of the micro-CT image quality phantom assesses the scanner's ability to detect objects of various sizes. This low contrast resolution module contains test objects (cylindrical voids) that decrease in diameter. From the top and continuing in the counter clockwise direction, figure 5 depicts the two sets of six circular test objects (30µm, 25µm, 20µm, 10µm, 6µm, and 2µm). This test module evaluates the scanner's limitations of distinguishing diminishing contrast size. It is also a simple test of the resolution capabilities of an imaging system.

To fully characterize contrast discrimination performance, several parameters need be assessed. All other conditions being held constant, the scan should be performed at the lowest and highest mAs setting to ensure resolution factors do not vary with mAs. The same should be done in varying kVp, while holding all other parameters constant.

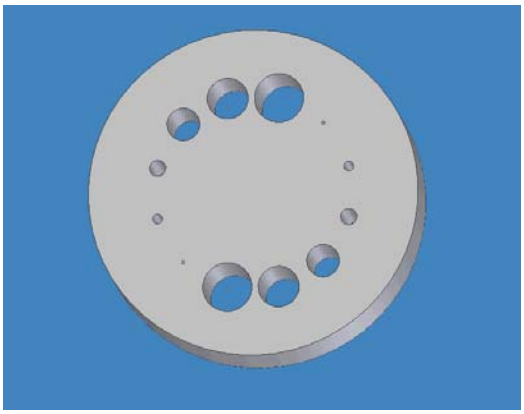

Figure 4.3.1-15: Visualization of the low-contrast resolution module.

Spatial resolution defines the ability of an imaging system to accurately depict objects in the three spatial dimensions of the image. The classic notion of spatial resolution is the ability of an image system to distinctly depict two objects as they become smaller and closer together. The closer they are, with the image still showing them as separate objects, the better the spatial resolution. At some point, the two objects become so close that they appear as one, and at this point spatial resolution is lost.

The spatial resolution module evaluates the ability of a micro-CT scanner to provide the sharpness or detail of a star pattern test object. This fourth module is again 50µm thick and 200µm in diameter, but contains a star pattern of six intersecting resolution bars. Each bar (or void) is 180µm long, 20µm wide, and extends the full 50µm of the module's thickness (Figure 4.3.1-6). The gap length between adjacent lines can thus be measured. It is the last gap distance, measurable before adjacent lines become indistinguishable, that is recorded as the system's spatial resolution limit.

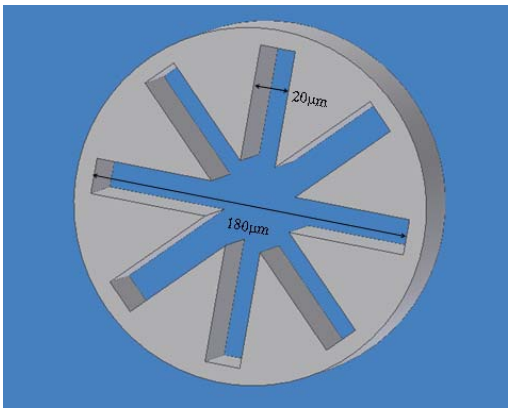

Figure 4.3.1-16: Visualization of the high-contrast resolution module

The micro-CT phantom developed at the University of Florida allows for a comprehensive evaluation of a micro-CT system's performance with regard to spatial uniformity, low contrast sensitivity, and spatial resolution. As the fabrication scale of MEMS devices decreases, the level of sophistication of device architecture and operations continues to increase. The completed photo-mask is illustrated in Figure 4.3.1-18. The expansion to complex three-dimensional structures necessitates the improvement of evaluation tools that can monitor both the assembly process and device functionality of Micro-Electro-Mechanical Systems.

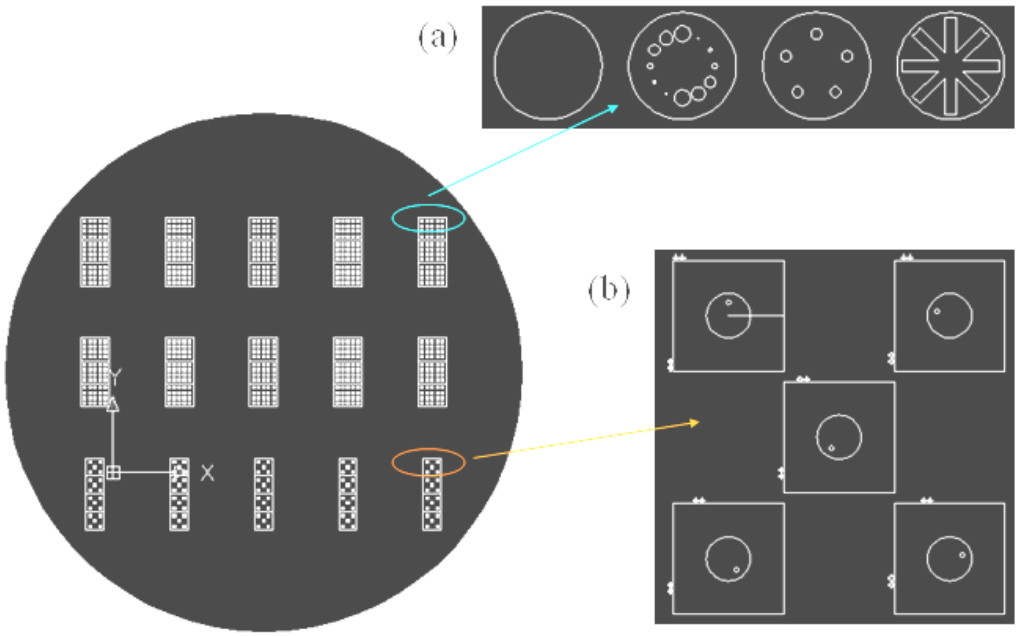

Figure 4.3.1-17: Details of the photo-mask designed and produced to construct the micro-CT standard test object.

The results obtained from these studies provide a series of useful tools to aid in the NNSA's characterization and assembly of complex MEMS devices. We continue to better define optimized imaging techniques and tools for the specialized task of MEMS component imaging and visualization. These tools provide the foundations for developing an advanced imaging system that can be readily integrated into the robotics- assisted MEMS assembly process, ultimately providing consistent assembly and operation of complex MEMS systems.

4.3.4 References

[1] American Association of Physicists in Medicine, AAPM Report No. 1, *"Phantoms for Performance Evaluation and Quality Assurance of CT Scanners"* (AAPM, Chicago, Illinois, 1977).

[2] American Association of Physicists in Medicine, AAPM Report No. 39, *"Specification and Acceptance Testing of Computer Tomography Scanners"* (AAPM, New York, NY, 1993).

[3] J. T. Bushberg, J. A. Seibert, E. M. Leidholdt, J. M. Boone, "*The Essential Physics of Medical Imaging,"* (Lippincott Williams & Wilkins, Philadelphia, PA, 2002).

[4] P. C. Johns, M. Yaffe, *"Scattered Radiation for Fan Beams,"* Med. Phys., 9:231-239, (1982).

4.4 LEVEL-II: DEVELOPMENT OF MACRO AND MICRO FORCE CONTROL TECHNOLOGIES

4.4 Level II: Development of Macro and Micro Force Control Technologies

4.4.1 Objective

This research area is concerned with the control of contact forces at the micro and macro scale during in-contact robotic operations. At the micro scale, University of Florida researchers are investigating how force control technologies that incorporate tensegrity principles can be applied to the problem of micro-assembly. At the macro scale, the objective of this research is to develop passive and active mechanisms that incorporate compliance in order to control contact forces during manipulation tasks.

4.4.2 Description of Work Accomplished

4.4.2.1 Level III: Compliant Spatial Micro-Mechanisms

The research is concerned with how spatial micro-mechanisms can be fabricated in the plane and then be made to deploy to their spatial configuration. The work is based on prior UFL research in the area of tensegrity systems. These devices use compliance and internal stress to cause a device to deploy from a stowed configuration (in this case from a planar configuration) to a minimum energy configuration (spatial configuration).

Tensegrity structures are self-deployable. This fact allows the fabrication of the structure at the planar level and then allows it to jump to the three-dimensional space. Figure 4.4.2.1-1 illustrates this idea. The lower ends of a prismatic tensegrity structure with 3 struts were joined to the substrate using universal joints. Initially all ties and struts are parallel to the plane and the system remains in equilibrium due to the tension generated for some of its ties and the reactions of the supports. When a small force in the upper direction is applied, the system pops up in a sudden and chaotic movement to reach another equilibrium position but now a three-dimensional structure has been created.

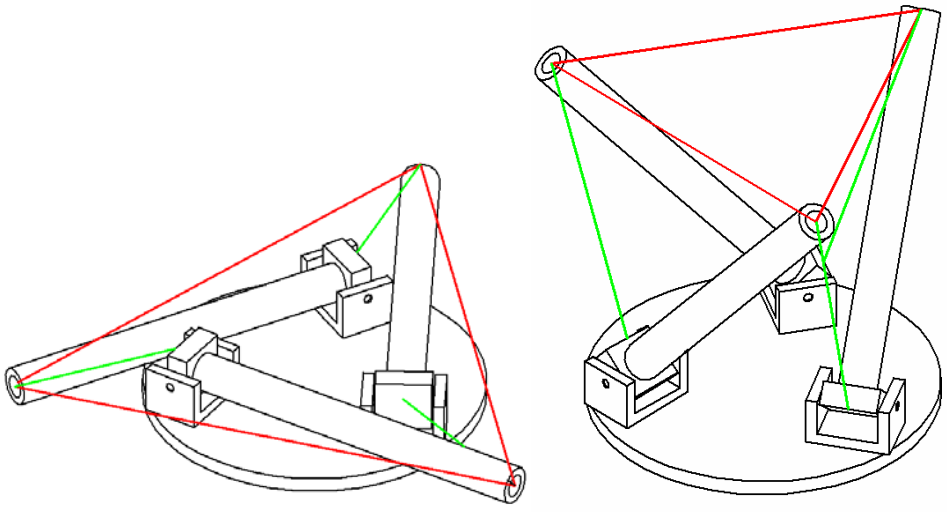

Figure 4.4.2.1-1 Self-Deployable Tensegrity Structure

Work at the beginning of the year focused on identifying candidate geometries and examining suitable materials and fabrication technologies to facilitate the development of this concept. Joint types at the micro-mechanical level are typically flexure types. Revolute types are permitted if the axis of rotation is normal to the plane of the substrate. A concept was developed that utilizes curved elements for the ridged links. A simple illustration is shown in figure 4.4.2.1-2

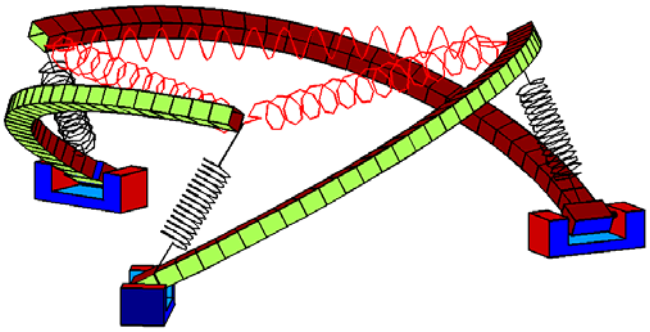

Figure 4.4.2.1-2 Self-Deploying Curved Link Tensegrity Structure

The curved links are to be fabricated such that their radius of curvature can be changed with thermal or electrical input. A mechanism that is a mechanical analogy of the proposed curved link device has been designed and prototyped. The goal of the exercise is to examine the feasibility of the concept. An unbalanced scissors type mechanism is used to simulate the expected motion of the curved micro actuator. The mechanism works as designed, and leads credibility to the research thrust. Figure 4.4.2.1-3 shows the mechanism.

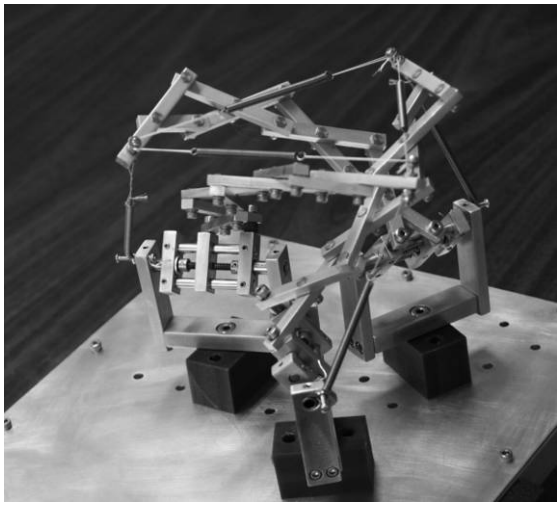

Figure 4.4.2.1-3 Self-Deploying Mechanical Analogy

Work has focused on the study of existing MEMS devices able to reach positions out of the plane has and on research to create a new device able to position an object in three-dimensional space. The next step is the detailed design of the system and its analysis and test.

It seems interesting to take advantage of the properties of the elastic systems to create a platform at the MEMS level. It can be thought as a tensegrity system that has been transformed in

order to adapt it to the micro manufacturing requirements. Tensegrity structures are formed by rigid and elastic elements that remain stable without the presence of external forces, as it is shown in Figure 4.4.2.1-4. The number of rigid elements shown here are six, but this is not a requirement.

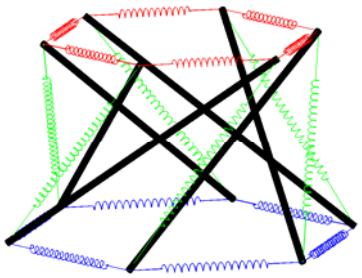

Figure 4.4.2.1-4 . Tensegrity structures with straight beams

This is a complex shape which requires complex manipulations, not affordable at the MEMS level. If the rigid and straight elements are replaced by curved beams, the stability still remains. Figure 4.4.2.1-5 displays a device with three struts which lower ends are connected to the substrate through 2-degrees of freedom joints.

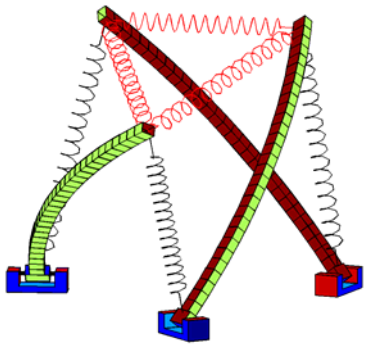

Figure 4.4.2.1-5 . Tensegrity structures with curved beams

The advantage of curved beams is that they can be achieved if each beam is made of 2 materials with different thermal expansion coefficient and increasing the temperature. This procedure has been used successfully in several micro devices.

The change of radius of curvature of each beam may provide a particular motion to the device that can be used for positioning a platform, like it is shown in Figure 4.4.2.1-6, where lateral ties are hidden for the sake of clarity.

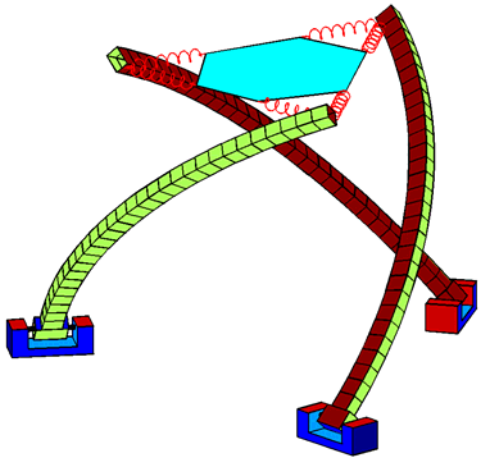

Figure 4.4.2.1-6. Device carrying a platform

Micro manufacturing techniques are very restrictive and joints with two degrees of freedom at the fixed ends are not easy to achieve. If the bimorph beams are arranged in such a way that the deformation is perpendicular to the substrate, a system like that shown in Figure 4.4.2.1-7 can be devised (ties and top platform are not shown).

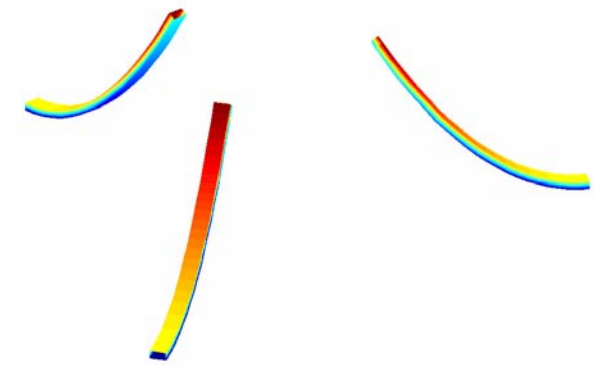

Figure 4.4.2.1-7. Scheme of a device with compliant joints

Manufacturing is simplified because there are no rigid joints, and the stiffness of the beams at the fixed ends replaces the task performed by the lateral ties, eliminating the lateral ties. Additional simplifications are being studied.

The device is worthy from the kinematics point of view, however in order to implement it, it is necessary to consider several aspects: compliances of the links, materials available for the ties and their properties and a kinematic model to predict the behavior of the device.

The detailed design of a new micro-scale device that can be fabricated in the plane and then deployed to three dimensions has been completed. The shape of the device can be controlled by applying a current that controls the bending of bi-material beams. The device is applicable to micro-manipulation tasks that are being investigated at the Sandia National Laboratory.

The project continues with the design of the device, the mathematical model for the mechanism and its manufacturing.

4.4.2.2. Design

The initial concept associated with a tensegrity system to obtain a device able to move out of the plane is valid but due to the limitations of the micro manufacturing techniques, it is necessary to introduce simplifications. It is known that if a beam is built with 2 materials with different thermal expansion coefficient, the beam bends when the temperature increases. Temperature can be increased with a resistor embedded in the beam. Materials selected for the bimorph beam are silicone dioxide and aluminum. Figure 4.4.2.1-8 shows a resistor that is created on the silicone dioxide layer, (upper part of the beam is not displayed, and device is not a scale). In this way a change in voltage creates a change of curvature of the beam.

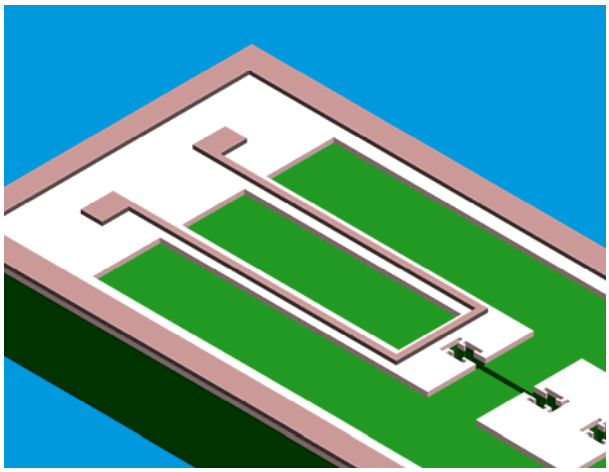

Figure 4.4.2.1-8: Detail of a resistor on the beam

If a set of these beams is connected to a central platform through compliant elements, it is possible to control the position and the orientation of the platform just varying the voltage applied to the beams. Figure 4.4.2.1-9 presents the concept of a platform actuated by two beams (the device is not a scale).

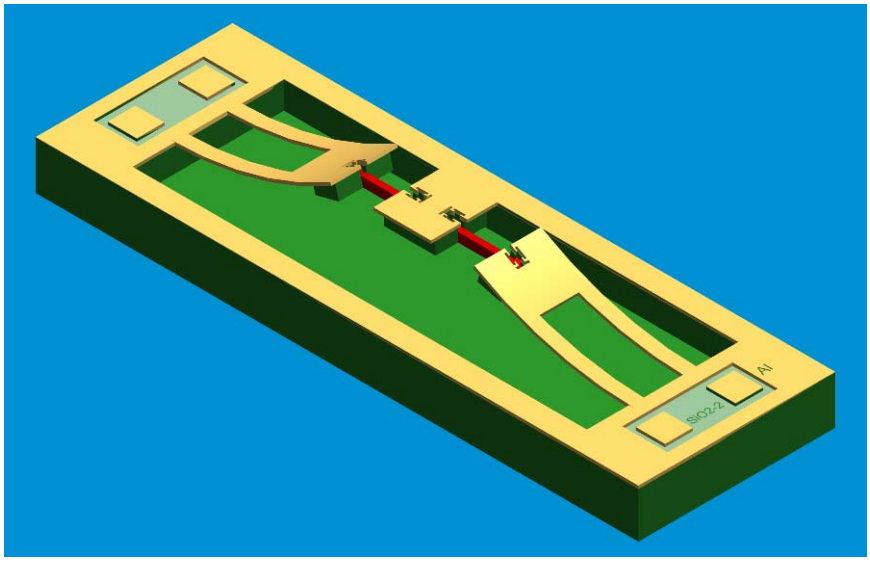

Figure 4.4.2.1-9: Platform actuated by two bimorph beams

4.4.2.3 Mathematical Model

The motion of the platform is complex due to the presence of compliant elements. A mathematical model must be developed in order to understand the behavior of the system. For this purpose two problems are formulated for a platform actuated by 3 beams: forward and reverse analysis. There are several ways to pose the reverse analysis problem.

- Forward analysis: given the position of the free ends of the beams with respect to a fixed coordinate system, find the position and the orientation of the platform.
- Reverse analysis: Given the orientation of the platform and the location of one of the free ends of the beams, find the location of the other two ends of the beams.

Both problems were solved using the Newtonian approach. In each case a set of nonlinear equations results, which are solved using numerical methods.

4.4.2.4 Manufacturing

Once the general features of the design have been established and there is a tool to predict the behavior of the device, the next step is the construction of the mechanism. Ideally this step would include the definition of the all the details, however there are many issues that only can be solved by experimentation. Micro manufacturing techniques used here consist basically on adding and removing material using plasma etching. Etching processes are strongly dependent on chemical composition of plasma, parameters assigned to the machines, materials being processed and geometry of the parts. Therefore it is not always possible to predict the exact behavior of a process and tests are required.

A set of masks were created with the geometry of the desired device but with different dimensions. Figures 4.4.2.1-10 - 12 display one of the masks used and details of several features.

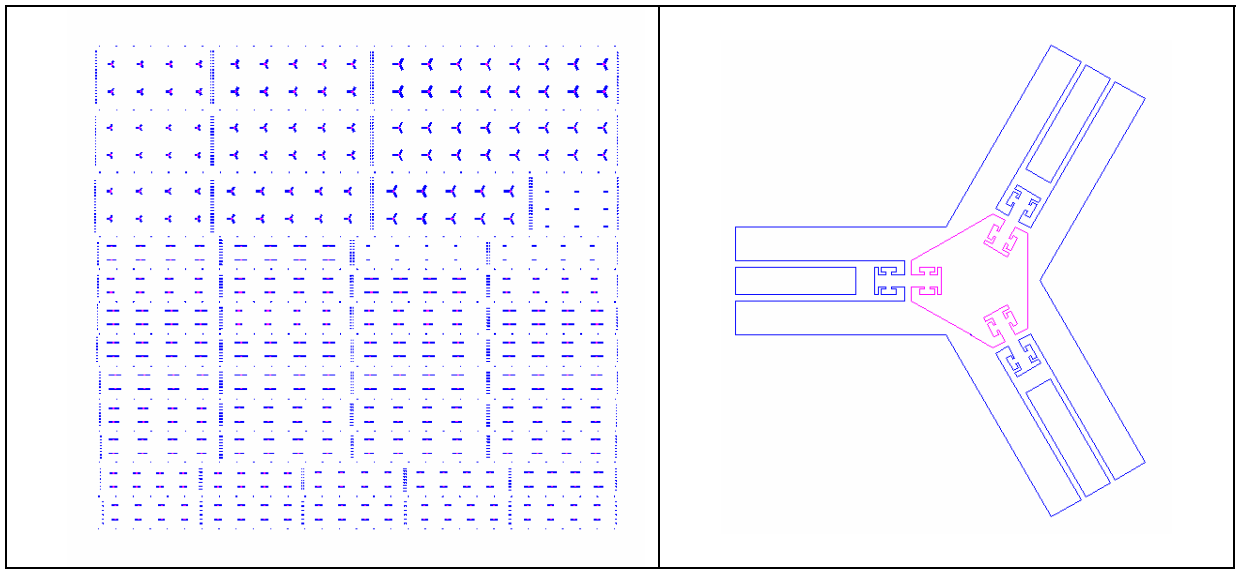

Figure 4.4.2.1-10: Mask and detail of one of the features.

Typical mask size allows numerous MEMS devices. The masks include families of designs with varied parameters, to allow more precise design revision. The illustrations that follows depicts several of the modeled designs.

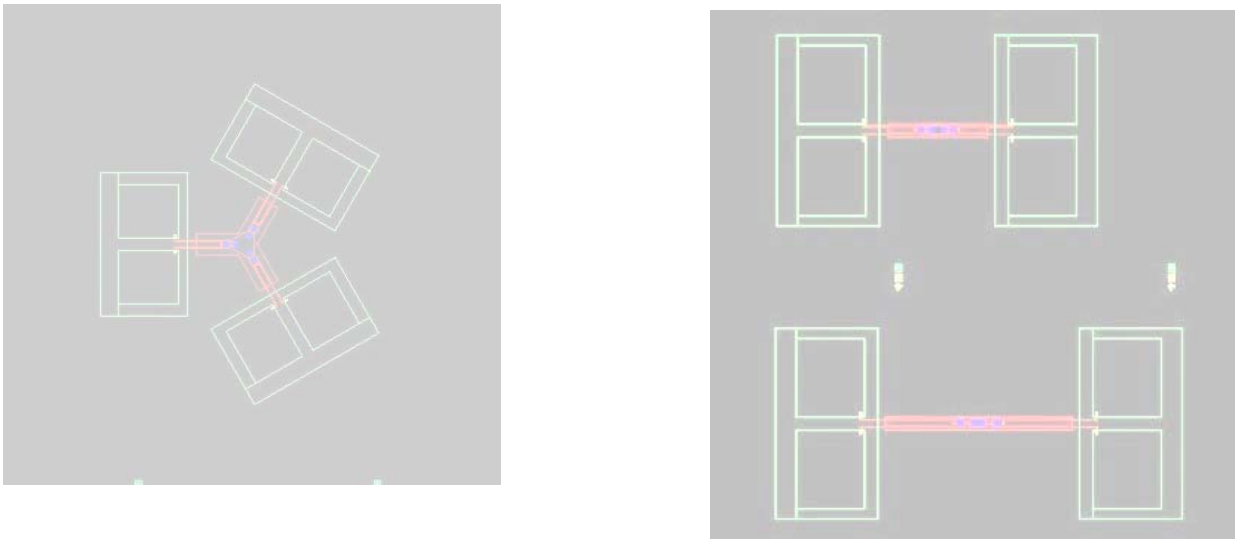

Figure 4.4.2.1-11: Illustrations of self deployable MEMS devices

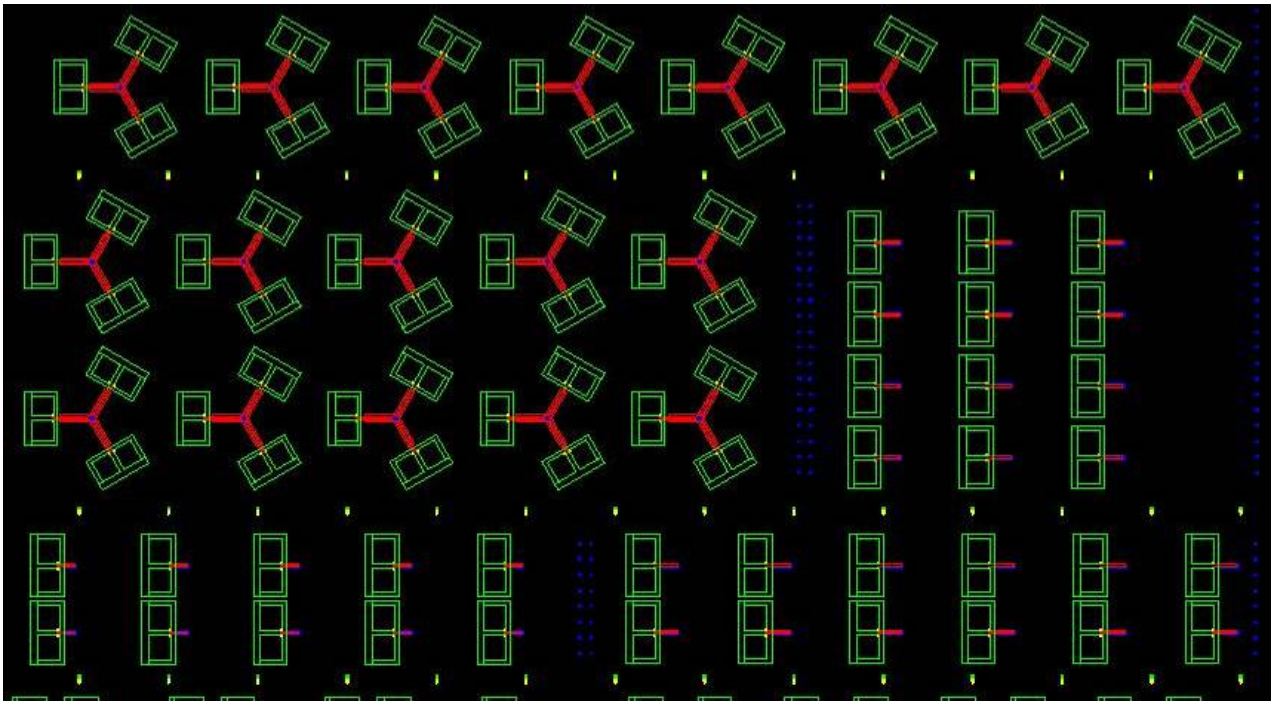

Figure 4.4.2.1-12: Section of top layer of mask for self deployable MEMS devices.

Masks were designed using software for 3-D modeling and the final result exported to a conventional 2-D format. After solving compatibilities problems between software used by the manufacturer and the software used for the design, the masks are built.

With these masks and after training in lab equipments handling, wafers are processed in and basic features are obtained. The next step is to study the behavior of the elastomeric material used for the ties of the device. With all the information gathered from the experiments which include etching rates, distribution of the elements, most desirable geometries and general aspects associated with the manipulation of the equipment, it is possible to proceed to final design, which is the coming step.

4.4.3 Description of Adaptive Compliant Work Accomplished

4.4.3.1 Level III: Adaptive Compliant Mechanisms

This research is focused on the analysis of planar and spatial mechanisms whose compliance characteristics can be modified and controlled. A prototype passive compliant coupling has been developed at UFL for application as a wrist element on an industrial robot. A control scheme has been designed that moves the distal end of the manipulator in order to control the sensed applied loading on the compliant coupling.

Current work includes examination of the stiffness mapping for two serially arranged parallel compliant devices. The investigation of an application of the compliant wrist element was also initiated. The wrist element has been mounted on a Puma industrial robot, and integration with the controller begun.

Several areas of the kinestatic controls problem have been investigated to date. These involve testing of both the Puma manipulator as well as the specialized Stewart platform intended for force control. Both software and hardware testing have been performed to evaluate the behavior and performance of these mechanisms. Also, some design work has begun on methods to easily obtain measurements from the platform that could potentially expand its effective workspace.

The Puma manipulator is primarily intended to actuate the base of the Stewart platform to obtain a desired pose and wrench. Therefore, the current controller for the robot has been tested to determine the accuracy of motion. This has revealed some errors in the controller implementation that lead to undesirably high inaccuracies. However, it is believed that development of a new interface program should correct these difficulties.

The Stewart platform has been the primary focus of testing and analysis as it is the most critical piece in the force control problem. Physical testing of the platform was performed to measure the effects of leg hysteresis on positioning and force application accuracy. The results show that very slight errors are present due to hysteresis. The plan is to implement dithering to the mechanism to reduce the positional errors below current sensor resolution. Calculations show that this should improve force accuracy to acceptable limits.

Software is being developed to evaluate the effects that slight errors in predicted positioning will have on the general stiffness matrix and thus on the applied wrench. This will be used to determine the best way to measure the actual dimensions of the platform and its legs. This software could also be useful in developing an efficient control scheme as well as predicting the effects that leg masses will have on the modeling of the mechanism.

Examination of the stiffness mapping for two serially arranged parallel compliant devices has been completed. Serially arranged parallel compliant mechanisms are candidates for developing variable compliance devices. Figure 4.4.2.2-1 illustrates the serial arrangement of the parallel compliances.

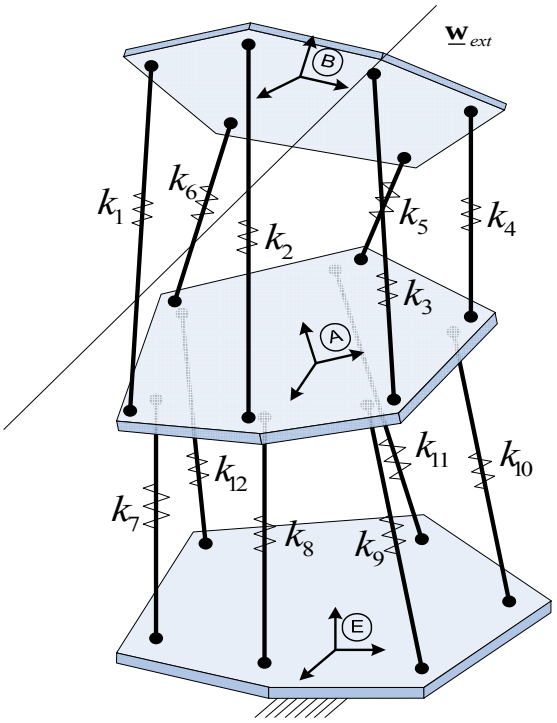

Figure 4.4.2.2-1: Serially Connected Parallel Compliances

Figure 4.4.2.2-1 depicts the compliant mechanism whose stiffness matrix is found. Body A is connected to ground by six compliant couplings and body B is connected to body A in the same way. Each compliant coupling has a spherical joint at each end and a prismatic joint with a spring in the middle. It is assumed that an external wrench $\underline{\mathbf{w}}_{ext}$ is applied to body B and that both body B and body A are in static equilibrium. The poses of body A and body B and the spring constants and free lengths of all compliant couplings are known.

The stiffness matrix $[K]$ which maps a small twist of the moving body B in terms of the ground, ${}^{E}\delta\underline{\mathbf{D}}^{B}$ (written in axis coordinates), into the corresponding wrench variation, $\delta\underline{\mathbf{w}}_{ext}$ (written in ray coordinates), is desired to be derived and this relationship can be written as

$$\delta\underline{\mathbf{w}}_{ext} = [K]\,{}^{E}\delta\underline{\mathbf{D}}^{B} . \qquad (1a)$$

The stiffness matrix will be derived by taking a derivative of the static equilibrium equations of body A and body B as

$$\underline{\mathbf{w}}_{ext} = \sum_{i=1}^{6}\underline{\mathbf{w}}_i = \sum_{i=7}^{12}\underline{\mathbf{w}}_i \qquad (2a)$$

$$\delta\underline{\mathbf{w}}_{ext} = \sum_{i=1}^{6}\delta\underline{\mathbf{w}}_i = \sum_{i=7}^{12}\delta\underline{\mathbf{w}}_i \qquad (3a)$$

where $\underline{\mathbf{w}}_i$ are the wrenches from the compliant couplings.

The research arrived at the following expression for the stiffness mapping:

$$[K]=[K_F]_{R,L}\left([K_F]_{R,L}+[K_F]_{R,U}+(\underline{\mathbf{w}}_{ext}\times)\right)^{-1}[K_F]_{R,U} \quad (4a)$$

$[K_F]$ is the stiffness matrix of a spatial compliant coupling and maps a small twist of a body into the corresponding variation of the wrench. The subscripts $_{R,L}$ and $_{R,U}$ differentiate between the upper and lower parallel compliant mechanisms. $\underline{\mathbf{w}}_{ext}\times$ is the external wrench expressed as a spatial cross product operator.

A derivative of the spring wrench connecting two moving bodies was developed by using screw theory and an intermediate frame and applied to obtain the stiffness matrix of a mechanism having two compliant parallel mechanisms in a serial arrangement. It was shown that a derivative of the spring wrench connecting two moving bodies depends not only on a relative twist between the two bodies but also on the twist of the intermediate body in terms of the inertial frame.

The derived stiffness matrix showed that the resultant compliance of two serially arranged parallel mechanisms is not the summation of the compliances of the constituent mechanisms unless the external wrench applied to the mechanism is zero. This result is a revision of the currently held formulation for compliance of serially connected mechanisms. This result also may be applied for mechanisms having arbitrary number of parallel mechanisms in a serial arrangement. This analysis is necessary to examine the usefulness of serially arranged parallel compliances in producing variable compliance devices. These results extend the understanding of compliance and are relevant to any realistic compliance application. The results of this research are being prepared for publication.

4.4.3.2 Adaptive Compliant Mechanisms: Parallel Planar Mechanism

A planar parallel mechanism with variable compliance was investigated, and the results presented. The mechanism consists of rigid bodies joined by adjustable compliant couplings. Each adjustable compliant coupling has a revolute joint at each end and a prismatic joint with an adjustable spring in the middle. The adjustable springs are assumed to be able to change their spring constants and free length. A control method to modulate the compliance of the mechanism while regulating the pose of the mechanism was studied.

4.4.3.3 Stiffness Matrix and Its Constraints of Planar Compliant Parallel Mechanisms

Static equilibrium equation of a compliant parallel mechanism under an external wrench $\underline{\mathbf{w}}_{ext}$ may be expressed as

$$\underline{\mathbf{w}}_{ext}=\sum_{i=1}^{N}\underline{\mathbf{f}}_i \quad (5)$$

where $\underline{\mathbf{f}}_i$ is the spring wrench of i-th compliant coupling and N is the number of legs of the mechanism. From the previous research result, a derivative of Eq. **Error! Reference source not found.** may be written as

$$\begin{aligned}\delta\underline{\mathbf{w}}_{ext}&=\sum_{i=1}^{N}\delta\underline{\mathbf{f}}_i\\&=\left(\sum_{i=1}^{N}[K_F]_i\right)^{E}\delta\underline{\mathbf{D}}^{A}\end{aligned} \quad (6)$$

where

$$[K_F]_i=k_i\underline{\$}_i\underline{\$}_i^{T}+k_i(1-\frac{l_{oi}}{l_i})\frac{\partial\underline{\$}_i}{\partial\theta_i}\frac{\partial\underline{\$}_i'^{T}}{\partial\theta_i}. \quad (7)$$

k_i, l_{oi}, l_i, and θ_i in Eq. **Error! Reference source not found.** are the spring constant, the spring free length, the current spring length, and the rising angle of ith compliant coupling. In addition, $\underline{\$}_i$ represents the unitized Plücker coordinates of the line along the ith compliant coupling and may be written explicitly as

$$\underline{\$}_i = \begin{bmatrix} \underline{\mathbf{S}}_i \\ \underline{\mathbf{r}}_{P,i} \times \underline{\mathbf{S}}_i \end{bmatrix} = \begin{bmatrix} \cos\theta_i \\ \sin\theta_i \\ r_{x,i}\sin\theta_i - r_{y,i}\cos\theta_i \end{bmatrix} \tag{8}$$

where $r_{x,i}$ and $r_{y,i}$ are the pivot position of ith compliant coupling in ground. Then Eq. **Error! Reference source not found.** leads to

$$\frac{\partial \underline{\$}_i}{\partial \theta_i} = \begin{bmatrix} -\sin\theta_i \\ \cos\theta_i \\ r_{x,i}\cos\theta_i + r_{y,i}\sin\theta_i \end{bmatrix}. \tag{9}$$

The stiffness matrix of the mechanism $[K]$ can be written from Eq. **Error! Reference source not found.** as

$$[K] = \sum_{i=1}^{N} [K_F]_i \,. \tag{10}$$

Ciblak and Lipkin (1994) showed that the stiffness matrix of compliant parallel mechanisms can be decomposed into a symmetric and a skew symmetric part and that the skew symmetric part is negative one-half the externally applied load expressed as a spatial cross product operator. For planar mechanisms, the skew symmetric part can be written as

$$\begin{aligned} [K] &= \frac{[K]+[K]^T}{2} + \frac{[K]-[K]^T}{2} \\ &= [K]_{Symmetric} + [K]_{Skew\ Symmetric} \end{aligned} \tag{11}$$

$$[K]_{Skew\ Symmetric} = \frac{[K]-[K]^T}{2} = -\frac{1}{2}\begin{bmatrix} 0 & 0 & f_y \\ 0 & 0 & -f_x \\ -f_y & f_x & 0 \end{bmatrix} \tag{12}$$

where $\underline{\mathbf{w}}_{ext} = \begin{bmatrix} f_x, f_y, m_z \end{bmatrix}^T$ is the external wrench.

It is important to note that no matter how many compliant couplings are connected and no matter how the spring constants and the free lengths of the constituent compliant couplings are changed the stiffness matrix of a compliant parallel mechanism contains only six independent variables and the stiffness matrix may be rewritten as

$$[K] = \begin{bmatrix} K_{11} & K_{12} & K_{13} \\ K_{12} & K_{22} & K_{32} + f_x \\ K_{13} + f_y & K_{32} & K_{33} \end{bmatrix}. \tag{13}$$

From Eqs. **Error! Reference source not found.-Error! Reference source not found.** the six independent elements of the stiffness matrix $[K]$ can be explicitly written as

$$K_{11} = \sum_{i=1}^{N} \left(k_i - k_i \frac{l_{oi}}{l_i} \sin^2\theta_i \right) \tag{14}$$

$$K_{12} = \sum_{i=1}^{N} \left(k_i \frac{l_{oi}}{l_i} \sin\theta_i \cos\theta_i \right) \tag{15}$$

$$K_{13} = \sum_{i=1}^{N} \left(-k_i (l_i \sin\theta_i + r_{y,i}) + k_i \frac{l_{oi}}{l_i} (l_i \sin\theta_i + r_{x,i} \sin\theta_i \cos\theta_i + r_{y,i} \sin^2\theta_i) \right) \tag{16}$$

$$K_{22} = \sum_{i=1}^{N} \left(k_i - k_i \frac{l_{oi}}{l_i} \cos^2\theta_i \right) \tag{17}$$

$$K_{32} = \sum_{i=1}^{N} \left(k_i r_{x,i} - k_i \frac{l_{oi}}{l_i} (r_{x,i} \cos^2\theta_i + r_{y,i} \sin\theta_i \cos\theta_i) \right) \tag{18}$$

$$K_{33} = \sum_{i=1}^{N} \left(\begin{array}{l} k_i r_{x,i} (l_i \cos\theta_i + r_{x,i}) + k_i r_{y,i} (l_i \sin\theta_i + r_{y,i}) \\ \quad - k_i \frac{l_{oi}}{l_i} r_{x,i} (l_i \cos\theta_i + r_{y,i} \sin\theta_i \cos\theta_i + r_{x,i} \cos^2\theta_i) \\ \quad - k_i \frac{l_{oi}}{l_i} r_{y,i} (l_i \sin\theta_i + r_{x,i} \sin\theta_i \cos\theta_i + r_{y,i} \sin^2\theta_i) \end{array} \right). \tag{19}$$

4.4.3.4 Stiffness Modulation by Using Adjustable Springs

It is desired to find an appropriate set of spring constants and free lengths of the constituent compliant couplings of a planar compliant parallel mechanism to implement a given stiffness matrix and to regulate the pose of the mechanism under a given external wrench.

It is important to note that the stiffness matrix contains only six independent variables and the equations for the independent variables are linear in terms of k_i's and $k_i l_{oi}$'s as shown in Eqs. **Error! Reference source not found.**-**Error! Reference source not found.** since all geometrical terms are constant. In addition to the equations for the stiffness matrix, the system should satisfy static equilibrium equations to regulate the pose of the mechanism and from Eqs. **Error! Reference source not found.** and **Error! Reference source not found.** it can be written as

$$\underline{\mathbf{w}}_{ext} = \begin{bmatrix} f_x \\ f_y \\ m_z \end{bmatrix} = \sum_{i=1}^{N} \left(k_i \left(l_i - l_{oi} \right) \begin{bmatrix} \cos\theta_i \\ \sin\theta_i \\ r_{x,i} \sin\theta_i - r_{y,i} \cos\theta_i \end{bmatrix} \right). \tag{20}$$

Eq. **Error! Reference source not found.** consists of three equations which are also linear in terms of k_i's and $k_i l_{oi}$'s. Since there are nine linear equations to be fulfilled and each adjustable compliant coupling possesses two control variables such as spring constant and free length, at least five adjustable compliant couplings are required.

The nine equations may be written in matrix form as

$$[A]\underline{\mathbf{X}} = \underline{\mathbf{B}} \tag{21}$$

where

$$\underline{\mathbf{B}} = \left[K_{11}, K_{12}, K_{13}, K_{22}, K_{32}, K_{33}, f_x, f_y, m_z \right]^T \tag{22}$$

$$\underline{\mathbf{X}} = \left[k_1, k_2, \cdots, k_N, k_1 l_{o1}, k_2 l_{o2}, \cdots, k_N l_{oN} \right]^T \tag{23}$$

$$[A]=\begin{bmatrix} 1 & 1 & \cdots & 1 & G_{1,1} & G_{1,2} & \cdots & G_{1,N} \\ 0 & 0 & \cdots & 0 & G_{2,1} & G_{2,2} & \cdots & G_{2,N} \\ G_{3,1} & G_{3,2} & \cdots & G_{3,N} & G_{4,1} & G_{4,2} & \cdots & G_{4,N} \\ 1 & 1 & \cdots & 1 & G_{5,1} & G_{5,2} & \cdots & G_{5,N} \\ G_{6,1} & G_{6,2} & \cdots & G_{6,N} & G_{7,1} & G_{7,2} & \cdots & G_{7,N} \\ G_{8,1} & G_{8,2} & \cdots & G_{8,N} & G_{9,1} & G_{9,2} & \cdots & G_{9,N} \\ H_{1,1} & H_{1,2} & \cdots & H_{1,N} & H_{2,1} & H_{2,2} & \cdots & H_{2,N} \\ H_{3,1} & H_{3,2} & \cdots & H_{3,N} & H_{4,1} & H_{4,2} & \cdots & H_{4,N} \\ H_{5,1} & H_{5,2} & \cdots & H_{5,N} & H_{6,1} & H_{6,2} & \cdots & H_{6,N} \end{bmatrix} \tag{24}$$

and where

$$G_{1,i}=-\frac{\sin^2\theta_i}{l_i},\ G_{2,i}=\frac{\sin\theta_i\cos\theta_i}{l_i},\ G_{3,i}=-l_i\sin\theta_i-r_{y,i}$$

$$G_{4,i}=\sin\theta_i+\frac{r_{x,i}\sin\theta_i\cos\theta_i+r_{y,i}\sin^2\theta_i}{l_i},\ G_{5,i}=-\frac{\cos^2\theta_i}{l_i}$$

$$G_{6,i}=r_{x,i},\ \ G_{7,i}=\frac{-r_{x,i}\cos^2\theta_i-r_{y,i}\sin\theta_i\cos\theta_i}{l_i}$$

$$G_{8,i}={r_{x,i}}^2+{r_{y,i}}^2+l_i(r_{x,i}\cos\theta_i+r_{y,i}\sin\theta_i)$$

$$G_{9,i}=-r_{x,i}\cos\theta_i-r_{y,i}\sin\theta_i-\frac{{r_{x,i}}^2\cos^2\theta_i+{r_{y,i}}^2\sin^2\theta_i+2r_{x,i}r_{y,i}\sin\theta_i\cos\theta_i}{l_i}$$

$$H_{1,i}=l_i\cos\theta_i,\ H_{2,i}=-\cos\theta_i,\ H_{3,i}=l_i\sin\theta_i,\ H_{4,i}=-\sin\theta_i$$

$$H_{5,i}=l_i\left(r_{x,i}\sin\theta_i-r_{y,i}\cos\theta_i\right),\ H_{6,i}=-\left(r_{x,i}\sin\theta_i-r_{y,i}\cos\theta_i\right).$$

It is important to note that $[A]$, $\underline{\mathbf{X}}$, and $\underline{\mathbf{B}}$ are 9 × (2**N*), (2**N*) × 1, and 9 × 1 matrices, respectively, where *N* denotes the number of the adjustable compliant couplings.

It is required to solve Eq. **Error! Reference source not found.** where the number of columns of matrix $[A]$ is in general greater than that of rows and the general solution $\underline{\mathbf{X}}_{sol}$ can be written as

$$\begin{aligned}\underline{\mathbf{X}}_{sol}&=\underline{\mathbf{X}}_p+\underline{\mathbf{X}}_h\\&=\underline{\mathbf{X}}_p+[A_{Null}]\underline{\mathbf{C}}\end{aligned} \tag{25}$$

where $\underline{\mathbf{X}}_p$, $\underline{\mathbf{X}}_h$, $[A_{Null}]$, and $\underline{\mathbf{C}}$ are the particular solution, the homogeneous solution, the null space of matrix $[A]$, and the coefficient column matrix, respectively (see Strang 1988). Once a solution $\underline{\mathbf{X}}_{sol}$ is obtained, l_{oi}'s are calculated from k_i's and $k_i l_{oi}$'s in $\underline{\mathbf{X}}_{sol}$. It is important to note that $[A_{Null}]$ is (2**N*) × (2**N*-9) matrix and $\underline{\mathbf{C}}$ is (2**N*-9) × 1 column matrix.

There might be many strategies to select the matrix $\underline{\mathbf{C}}$ which leads to a specific solution. For instance, if the norm of $\underline{\mathbf{X}}_{sol}$ is desired to be minimized, then by using projection matrix $[A_{Null-P}]$ (see Strang 1988), the solution can be obtained as

$$\underline{\mathbf{X}}_{Min.sol}=\underline{\mathbf{X}}_p+[A_{Null-P}]\left(-\underline{\mathbf{X}}_p\right) \tag{26}$$

where

$$[A_{Null-P}] = [A_{Null}]\left([A_{Null}]^T [A_{Null}]\right)^{-1} [A_{Null}]^T . \quad (27)$$

For another case, we might want the solution closest to a desired solution $\underline{\mathbf{X}}_d$ which may be constructed from operation ranges of adjustable compliant couplings, for instance, minimum and maximum spring constant and free length. Then, the solution can be obtained as

$$\underline{\mathbf{X}}_{d.sol} = \underline{\mathbf{X}}_p + [A_{Null-P}]\left(\underline{\mathbf{X}}_d - \underline{\mathbf{X}}_p\right). \quad (28)$$

Unfortunately, these methods involve mixed unit problems and do not guarantee a solution consisting of only positive spring constants and free lengths.

4.4.3.5 Adaptive Compliant Mechanisms: Variable Damping

This research concentrates on the geometric stability of parallel platform based manipulators. The aim is to simulate a reconfigurable device that can attain any desired compliance matrix relationship (the compliance matrix relates the displacement of the top of the platform to the force/torque applied to the top of the platform). A variable-damping device will be used to adjust the damping of the connectors. The best candidate device used to achieve variable-damping is the magnetorheological (MR) damper.

Parallel kinematic mechanism simulations have been undertaken to examine the use of variable damping. Each leg of the 6 DOF parallel kinematic mechanism has a magnetorheological damper for damping. The magnetorheological damper was modeled in Simulink according to the Bingham plastic model. The input to the model is the relative velocity between the two masses (m_1 and m_2 in Figure 4.4.2.2-7) which the damper connects and the control current. In the simulations, the MR damper is assumed to respond very fast and the time delay associated with the damper's response time is ignored.

The MR damper is implemented in a two DOF leg model. The connector leg consists of an actuator in series with the MR damper-spring pair. The stiffness and the friction of the actuator are modeled as a spring-damper pair in parallel with a force element as shown in Figure 4.4.2.2-2.

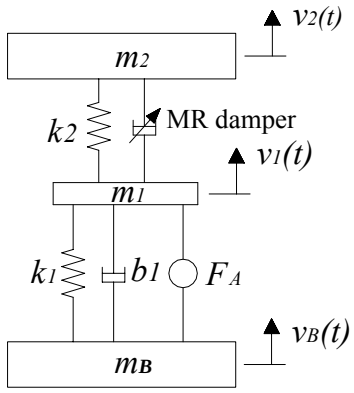

Figure 4.4.2.2-2. Two DOF platform leg model with MR damper

The two DOF leg system has the Bingham plastic model MR damper and an on/off control algorithm. In this algorithm, the MR damper is either turned on by applying a 2A input current or it is turned off by setting the input current to 0A. No intermediate current is applied. The bottom

mass (m_B) is subjected to a sinusoidal disturbance and the transmissibility between the top (m_2) and the bottom mass is calculated.

Figure 4.4.2.2-3 shows the transmissibility between the displacement of the top mass and the input excitation of a two DOF system. This model forms the basis of the connector legs of the six DOF platform system. The first mass, m_1, is the upper leg which would include the mass of the actuator piston and the MR damper. The second mass, m_2, is the portion of the parallel manipulator's top platform mass that a single leg has to carry. In this model, when a continuous 2A input current is applied to the MR damper, the link between the first mass, m_1, and the second mass, m_2, behaves almost as a rigid element. This is why the transmissibility is high for the first frequency, and the second peak is missing. On/off control reduces the peak at the first frequency and provides a lower transmissibility at higher frequencies.

The two DOF model previously described forms the basis of the connector legs of the six DOF platform system. The six DOF parallel platform mechanism can also be modeled in SimMechanics as shown in Figure 4.4.2.2-4. The bottom platform of the mechanism can be subjected to a sinusoidal excitation and the transmissibility of the top platform can be calculated. A drawing of the modeled parallel platform mechanism is shown in Figure 4.4.2.2-5.

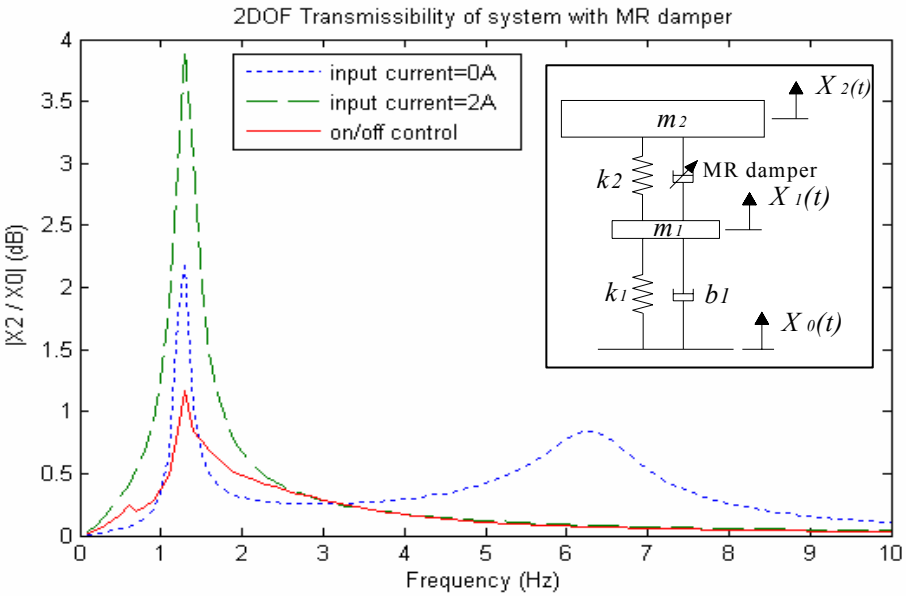

Figure 4.4.2.2-3. Transmissibility of the two DOF mass-spring-MR damper system with 0A input current, 2A input current, and on/off control (m1=5 kg, k1=2000 N/m, b1=10 Ns/m, m2=20 kg, k2=5000 N/m)

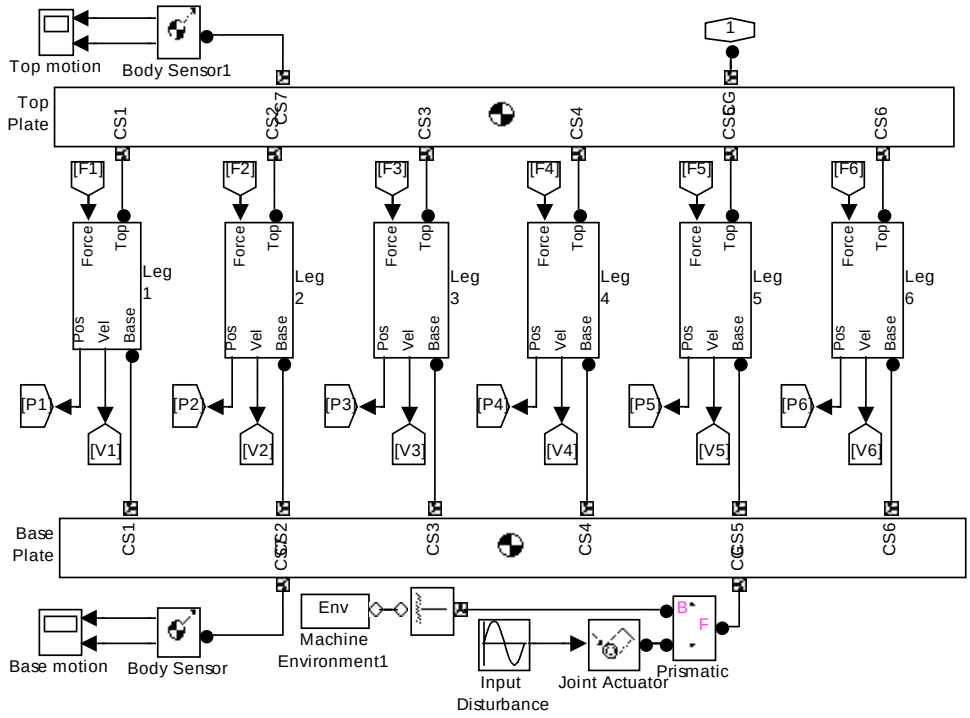

Figure 4.4.2.2-4. SimMechanics model of the six DOF model with sinusoidal excitation on the bottom platform

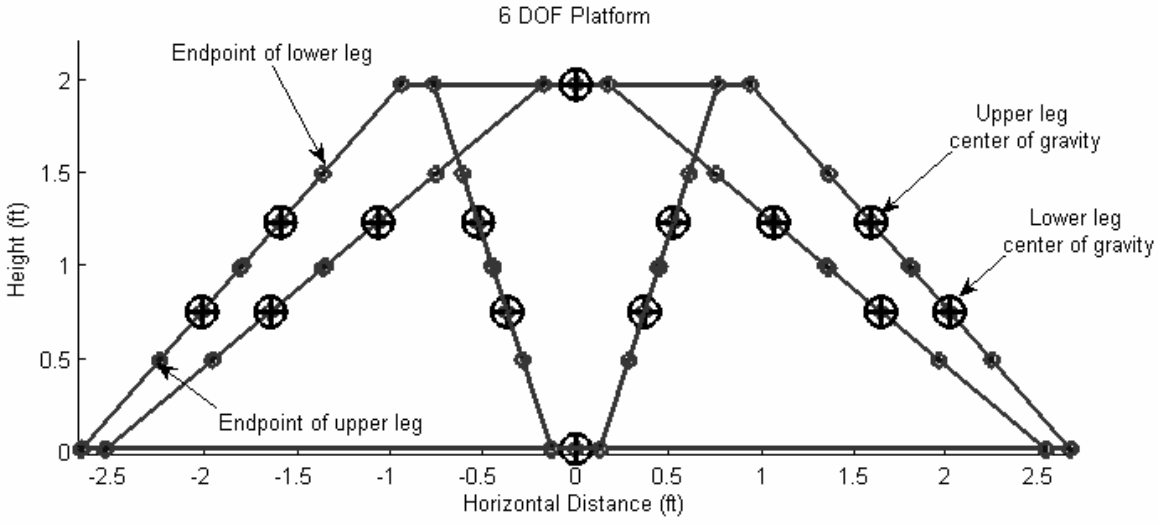

Figure 4.4.2.2-5. Six DOF parallel platform mechanism

4.4 References

Ball, R. S., 1900, "*A Treatise on the Theory of Screws*," Cambridge University Press, Cambridge, UK.

Ciblak, N., and Lipkin, H., 1994, "*Asymmetric Cartesian Stiffness for the Modeling of Compliant Robotic Systems,*" Proc. ASME 23rd Biennial Mech. Conf., Des. Eng. Div., Vol. 72, pp. 197-204, New York, NY.

Crane, C. D., Rico, J. M., and Duffy, J., 2006, "*Screw Theory and Its Application to Spatial Robot Manipulators,"* Cambridge University Press, Cambridge, UK.

Griffis, M., 1991, "*A Novel Theory for Simultaneously Regulating Force and Displacement,"* Ph.D. dissertation, University of Florida, Gainesville, FL.

Strang, G., 1988, "*Linear Algebra and Its Applications,"* Harcourt Brace Jovanovich, New York.